Multiple Integrated Antennas for Wearable Fifth-Generation Communication and Internet of Things Applications

CHIA-TE LIAO [ID] 1, ZHE-KAI YANG 2, AND HUA-MING CHEN [ID] 2, (Senior Member, IEEE)

[1] Department of Aviation Communication and Electronics, Air Force Institute of Technology, Kaohsiung 820, Taiwan
[2] Institute of Photonics Engineering, National Kaohsiung University of Science and Technology, Kaohsiung 807, Taiwan

Corresponding author: Chia Te Liao (jiader0502@gmail.com)

ABSTRACT This paper proposes integrating multiple antennas into wearable devices for application in fifth-generation (5G) communications and the Internet of Things (IoT). The frequency bands covered were wireless local area network 2.4-GHz/5-GHz channels (2410–2484 MHz), the global positioning system (1575 MHz), narrowband IoT band 8 (880–960 MHz), Global System for Mobile Communications 850/900, and the 5G frequency range 1 n77/78/79 band (3300–5000 MHz). The antennas were configured as a 2×2 multiple-input multiple-output system (MIMO). The antenna resonance contribution integrates the slot mode, monopole mode of the three-dimensional frame, and loop coupling monopole mode. The configuration of the independent matching circuits facilitated the effective control of the desired mode and the coverage of the desired bands. All integrated antennas were placed in a watch device ($37 \times 43 \times 8$ mm^3) with a metal body and a metal strap. An integrated miniaturized antenna was designed. The diversity gain and multiplexing efficiency between the MIMO antennas were 9.97dB and above -2dB, respectively. Favorable diversity performance was confirmed. The channel capacity of the 2×2 MIMO array was determined to be 8.8 bps/Hz. Moreover, its performance was evaluated through the addition of a hand tissue module. The impact of metal straps on antenna radiation performance was discussed. The specific absorption rate (SAR) was examined, and the best results obtained under an SAR of 1 g and 10 g were 0.25 and 0.58 W/kg, respectively. The findings demonstrate the suitability of the antenna for practical applications in 5G communication systems and the IoT.

INDEX TERMS Wearable computers, multiple-input multiple-output, metal frame, metal strap, impedance matching.

I. INTRODUCTION

With the rapid development of mobile communications, the market for wearable devices is thriving. For example, use of smart watches as a consumer electronic is increasing rapidly with the development of low-power technology and the Internet of Things (IoT). Moreover, smart watch positioning can be used in data collection. Regarding the overall industry, wearable devices are part of the IoT. Real-time location systems (RTLS) can perform positioning based on radio signals. Global positioning system (GPS) technology can be used outdoors. Indoors, wireless local area network (WLAN) frequency bands can be used to obtain the received signal strength indicator. The current position can then be

calculated to form an accurate positioning system. Regarding the communication interfaces of wearable technology, devices are connected through Bluetooth to a mobile phone and linked to a mobile application. A cloud platform examines which devices are connected and merges data streams across multiple communication protocols and standards. Networking between smart devices is the future of technology and enables the seamless collection of data through devices. Through an autonomous mobile communication network, commands can be issued to control IoT devices such as lights, televisions, and other home appliances, as well as vehicle networking systems. The principal challenge in smart watches involves considering consumer needs. Wearable electronic devices are typically made of metal, a material that blocks wireless signal transmission and reception through electromagnetic shielding. Consequently, the design

The associate editor coordinating the review of this manuscript and approving it for publication was Stefan Schwarz [ID].

of the antennas within such devices involves various bottlenecks.

Most smart watches with a metallic exterior have been designed to work only in the 2.4-GHz WLAN channel [1]–[5]. With the evolution of communication systems, 2.4-GHz 2 × 2 multiple-input multiple-output (MIMO) systems have been developed [6], [7]; moreover, with advances in mobile communications technology, long-term evolution (LTE) frequency bands have been introduced [8]–[10]. Among mobile phones, the product category with the greatest competition, mobile communication devices with a metallic appearance [10]–[19] are the norm. Consumers also prefer tablet computers with a metallic exterior [20]–[23]. With the emergence of the fifth-generation (5G) mobile communication system, convenient wearable devices that have a metallic appearance and IoT functions are becoming increasingly popular. Energy consumption is a major concern in smart watches. In general, millimeter-wave frequency bands are not used in market production. The main advantages of dual-band Wi-Fi equipment are that the Wi-Fi signal is stronger and more stable and that the transmission speed is higher. Furthermore, the use of Wi-Fi can enhance the energy efficiency of wireless devices, thereby meeting requirements in high-definition and big data wireless transmission. The effects of the structure of human tissue on antenna performance in smart watches must be considered in antenna design and setup [24], as should the impacts of the metal strap. In this paper, four sets of antennas in smart watches are proposed for use in 5G communications technology. Experiments and simulations were conducted, and the results were analyzed. The frequency bands covered Global System for Mobile Communications (GSM) 850/900 (850–960 MHz), narrowband IoT (NB-IoT) band 8 (880–915 MHz), GPS (1575 MHz), WLAN 2.4-GHz/5-GHz bands, and 5G frequency range 1 (FR1) n77/n78/n79 band (3300–5000 MHz). The 5G FR1 n77/n78/n79 band was incorporated into a 2 × 2 MIMO array, which improves spectrum utilization.

II. ANTENNA CONFIGURATION AND MULTIPLE ANTENNA DESIGN

This section presents the structure of the wearable antenna system (2 × 2 MIMO for the 5G FR1 n77/78/79 band (Ant 1 and Ant 2), WLAN 2.4-GHz/5-GHz dual-band antenna (Ant 3), and the antenna for IoT and RTLS-related applications (Ant 4). In the following subsections, the design of individual antennas is introduced.

A. ANTENNA SYSTEM STRUCTURE

The antenna system was designed using Ansys HFSS software. Fig. 1 presents the geometry of the proposed antenna system. The system circuit board was made of FR4 substrate with a dielectric constant of 4.4 and a loss tangent of 0.024. The edge of the circuit board was surrounded by a 0.8-mm-thick metal frame. The proposed smart watch measured 37 × 43 × 8 mm^3, approximate
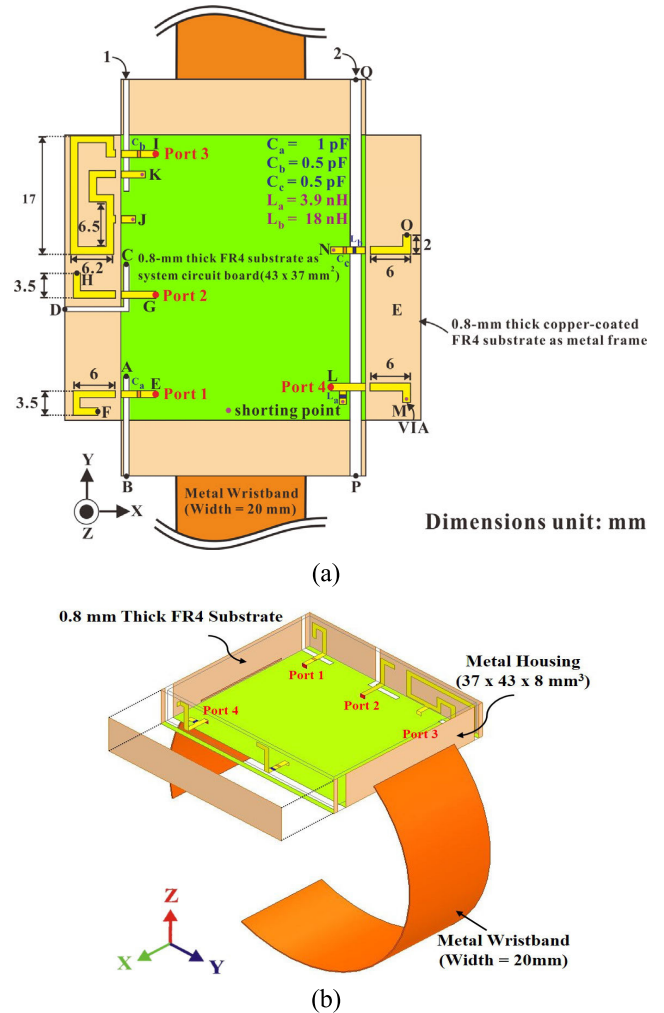

FIGURE 1. (a) Top view and (b) side view of the geometry of the proposed antenna system.

to the dimensions of the 44-mm Apple Watch Series 6. Given that the frequency band covered 850–5850 MHz (with the center frequency band being equal to 3350 MHz as the benchmark; 1 λ_0 = 89.55 mm), the overall electrical dimensions of this calculation method were 0.41 × 0.48 × 0.08 λ^3. Multiple integrated antenna systems suitable for wearable 5G communication applications, including Ant 1 and Ant 2 (5G FR1 n77/78/79 frequency bands), form a 2 × 2 MIMO configuration. Ant 3 covers the WLAN 2.4-GHz/5-GHz dual band, and Ant 4 covers the GSM 850/900, NB-IoT band 8 (880–915 MHz), and the GPS (1575 MHz). Four sets of antennas, which can be used to meet future market needs, are arranged in the interior of the smart watch on the long side; the space on the short side is left clear. Considering that the Apple Watch Series 6 has a replaceable strap made of leather, nylon, stainless steel, or ceramic, leaving this space clear can prevent the strap material (with different dielectric coefficients) from affecting transmission. Table 1 details the operating frequency bands corresponding to the long side of the watch.

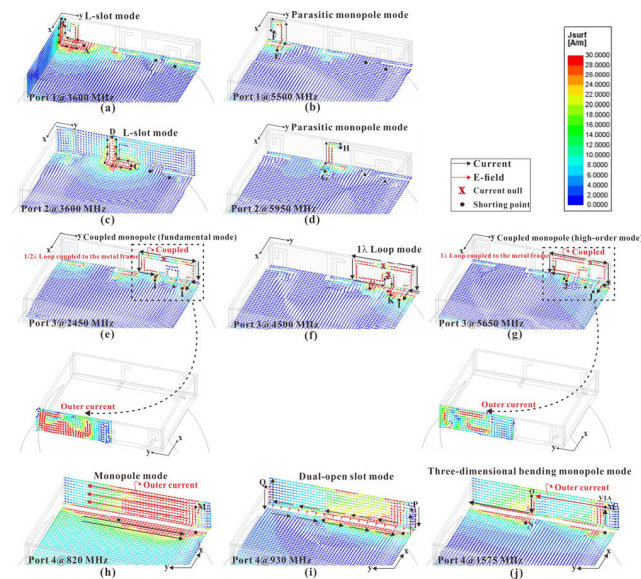| Band Antenna	Operation Frequency Bands	Application Index
Port 1	5G FR1 n77/n78/n79 band (3300MHz~5000 MHz)	5G system (2 × 2 MIMO)
Port 2	5G FR1 n77/n78/n79 band (3300MHz~5000 MHz)	
Port 3	WLAN 2.4 / 5G dual band (2400~2484MHz, 5150~5850MHz)	IoT and RTLS
Port 4	GSM850/900 (850MHz~960 MHz), NB-IoT band 8 (880~915 MHz), GPS (1575 MHz)	

FIGURE 2. Simulated vector current distributions of the antenna system. Port 1 is excited at (a) 3.6 GHz and (b) 5.5 GHz; port 2 is excited at (c) 3.6 GHz and (d) 5.95 GHz; port 3 is excited at (e) 2.4 GHz, (f) 4.5 GHz, and (g) 5.5 GHz; port 4 is excited at (h) 0.82 GHz, (i) 0.93 GHz, and (j) 1.575 GHz.

B. ANT 1 AND ANT 2 FOR MIMO CONFIGURATION

Fig. 1(a) displays the detailed structure of the antenna system. The red dot in the figure is the antenna feed point. The inner conductor of the 50-Ω coaxial cable is used for the connection. Ant 1 consists of a slot antenna and coupling line. The following is an explanation of each antenna. With Ant 1, the three-dimensional (3D) turning point in the wearable device is used to generate an L-shaped slot. The coupling line is used to excite the L-shaped slotted antenna, and the resonance path is from point A to point B. As indicated in Fig. 2(a), the resonance length is 15 mm, or approximately 0.14 wavelengths at 3600 MHz. The coupling line segment also forms a parasitic monopole antenna (strip EF). As displayed in Fig. 2(b), the resonance at 5550 MHz produces a double resonance mode that effectively covers the 5G FR1 n77/78/79 band in a small

space. Ant 2, which has the same structure as Ant 1, uses an L-shaped slotted antenna (slot CD). As shown in Fig. 2(c), the resonance length is 16 mm, which is approximately 0.15 wavelengths at 3600 MHz. The length of the coupling line (point G to point H) is also used for symbiosis with the metal frame. The same applies to the parasitic monopole antenna [Fig. 2(d)], which resonates at 5950 MHz. The coupling lines of Ant 1 (strip EF) and Ant 2 (strip GH) also contribute to the bandwidth ratio and the adjustment of impedance matching. Relevant details, including information on the parameters, are discussed in detail in Section III-B of this paper. The capacitance Ca (1 pF) of Ant 1 was used to fine-tune the impedance matching of the double resonance mode in the 5G FR1 n77/78/79 band.

C. ANT 3 for WLAN 2.4-GHz/5-GHz BAND

Consider a scenario in which the 2 × 2 MIMO dual antennas (Ant 1 and Ant 2) are configured on one side of the metal frame. Ant 3 was originally a loop antenna (point I to point J) designed to have dual load characteristics, as shown in Fig. 2(e). The total length of the bending loop is 47 mm. Coupling with the metal frame was the objective. The frame resonated out of the loop coupling monopole mode (i.e., the fundamental mode) at 2450 MHz. The same curved metal loop (point I to point J) resonated out of the loop coupling monopole mode (high-order mode) at 5650 MHz. The resonance path is indicated in Fig. 2(g). Because of the incomplete coverage of the WLAN 5G full band (5150–5850 MHz), for impedance matching, we further designed the bending loop (point I to point K) as a loop mode of one wavelength to resonate at 4500 MHz. This resonance mode was used to completely cover the bandwidth required in WLAN 5G applications. The resonance path is revealed in Fig. 2(f). In addition, lump capacitance C_b (0.5 pF) is used in conjunction with a curved path to form a distributed inductance (point I to point J) and a band-pass filter. The resonant frequency is calculated as follows:

$$f = \frac{1}{(2\pi \sqrt{L_{dis} C_b})} \quad (1)$$

In the internal structure, the line segment of the coupled monopole is from point I to point J, which can be regarded as a distributed inductor. The lumped capacitance C_b (0.5 pF) and the curved path, which can be calculated using equation (1), are used to form a distributed inductance (strip I→J) and a band-pass filter. This can be regarded as a distributed inductor. A dual-band band-pass filter can be used for analysis. Regarding series connection with a lumped capacitance C_b of 0.5 pF, L_{dis} is 8.1 nH at 2.5 GHz and 1.7 nH at 5.3 GHz. Thus, modal interference outside the WLAN 2.4-GHz/5-GHz frequency band was filtered out.

D. ANT 4 FOR GSM BAND/GPS BAND

Smart watches such as the Apple Watch Series 6 are sold in GPS and GPS + cellular models. In the GPS + cellular version, the Apple Watch need not be in the vicinity of
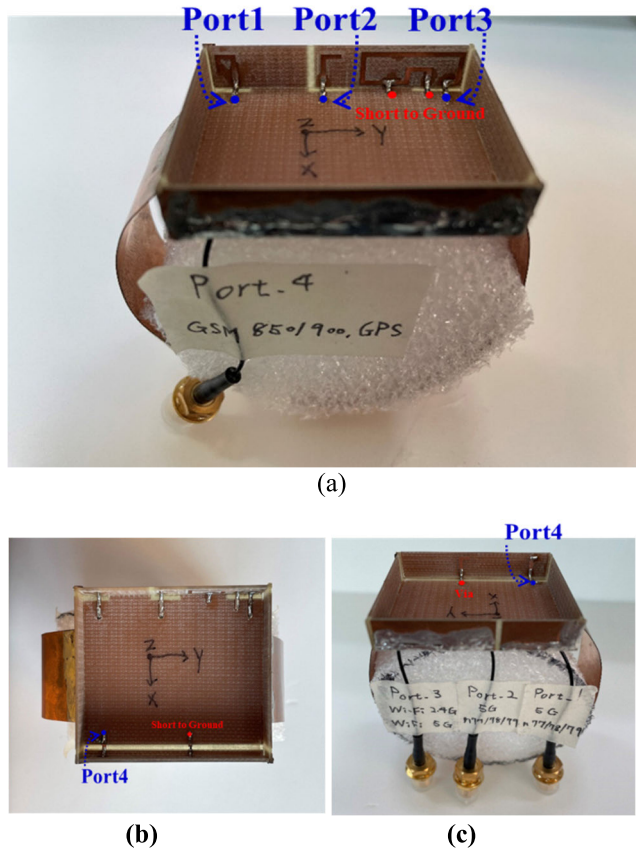
FIGURE 3. Multiple integrated antennas for wearable 5G communications applications: (a) overall configuration, (b) side view, and (c) alternate side view.

FIGURE 4. Simulated and measured reflection coefficients of the (a)Ant 1 and (b)Ant 2 in the 5G FR1 (n77/78/79) band.

the iPhone to execute communication functions, such as making calls and sending messages. The fourth antenna is mainly designed to cover the GSM 850/900 frequency band and GPS (1575 MHz) for mobile communication and satellite positioning, respectively. The design of the GSM frequency band, which has been directly fed to the metal frame, corresponding to point L–point M in [Fig. 1(a)], is introduced as follows. The selection of the resonant mode is presented in Fig. 2(h). The vibration length is approximately 56 mm, or approximately 0.15 times the λ_0 value of 820 MHz. This monopole resonance mode coexists with dual open slots (point P to point Q). As shown in Fig. 2(f), the resonance length is 59 mm or 0.14 wavelengths at 920 MHz. A double resonance mode was formed, and the GSM 850/900 frequency band was covered. The lumped inductance L_a (3.9 pF) in Ant 4 is used to adjust the impedance matching of the dual resonance mode generated in GSM 850/900. Adjustments can be made flexibly, according to actual applications. Regarding the resonance path in the GPS frequency band mode, from point L to point M, and through point O to point N, the lumped inductance L_b was used to reach the extended current path. As presented in Fig. 2(j), the current flows along the edge of the slot to form a 3D curved unipolar mode in which the metal frame and the slot
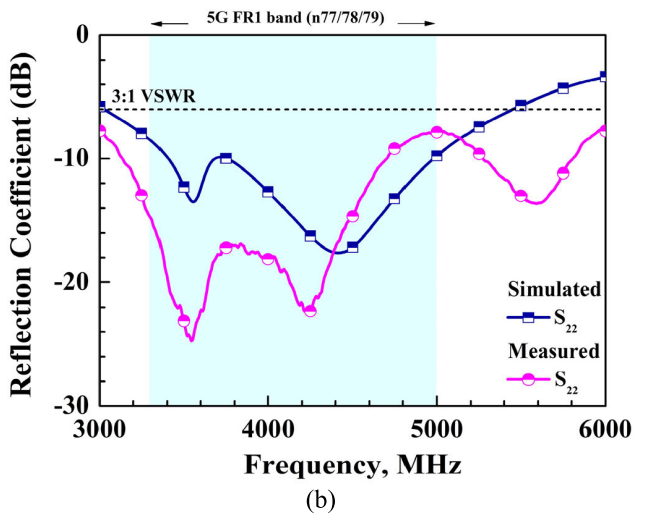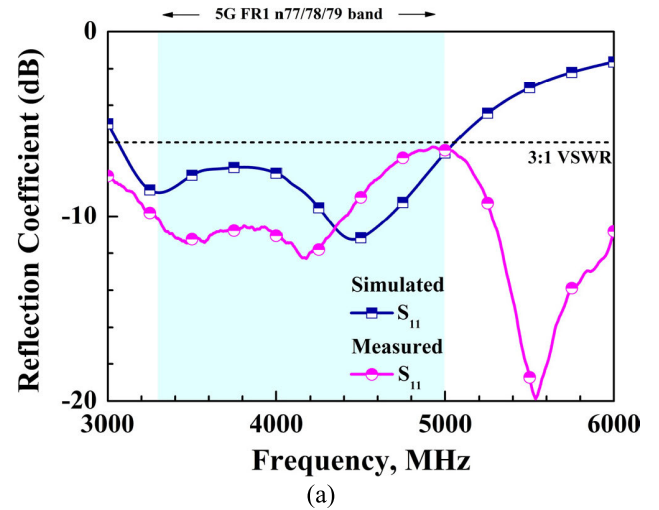
coexist. To form a band rejection filter function, a lumped capacitor C_c in series is used together with a lumped inductor L_b from point O to point N to ground.

III. RESULTS AND DISCUSSION
Experiments were conducted on the integrated antennas; the result for independent parameters are presented and discussed herein. Fig. 3 depicts a photograph of multiple integrated antennas for use in wearable 5G communication applications. As displayed in Fig. 4, both the simulated and measured reflection coefficients of Ant 1 and Ant 2 covered the 5G FR1 n77/78/79 band. Moreover, Fig. 5 demonstrates that the isolation between Ant 1 and Ant 2 in the design frequency band meets the commercial application standard of less than −10 dB. Figs. 6 and 7 present the simulated and measured reflection coefficients of Ant 3 and Ant 4, respectively. The slight difference in the simulation and measurement results is mainly due to small defects in the solder joints of the high-frequency substrate.
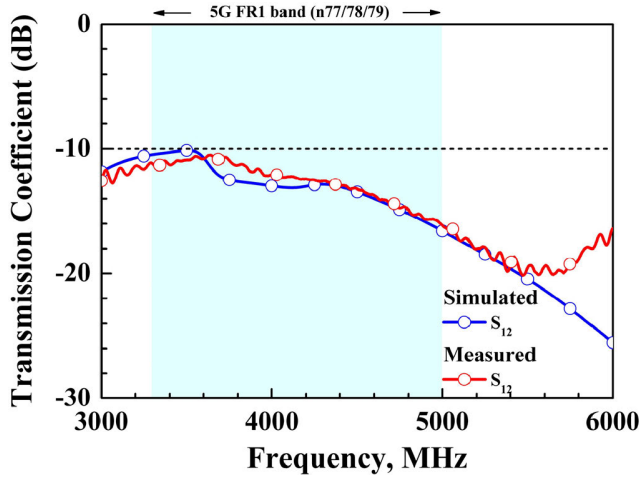
FIGURE 5. Simulated and measured transmission coefficients of the 5G FR1 n77/78/79 band in the 2 × 2 MIMO array.
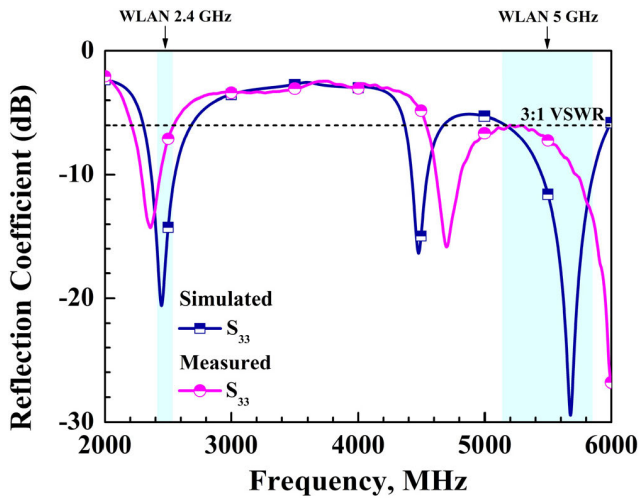

FIGURE 6. Simulated and measured reflection coefficients of the WLAN 2.4-GHz/5-GHz band.

FIGURE 7. (a) Simulated and (b) measured reflection coefficients of the GSM 850/900 and GPS 1575 bands.

A. SIMULATION AND MEASURED RESULTS

Fig. 8 shows the simulated and measured antenna radiation efficiency of Ant 1, Ant 2, Ant 3, and Ant 4 in each design frequency band. Fig. 8(a) and Fig. 8(b), which correspond to Ant 1 and Ant 2, respectively, indicate that the 5G FR1 n77/78/79 band helped achieve a favorable radiation efficiency of more than 45%, in line with commercial standards. The gain performance is between 1dBi∼4.2dBi. Regarding the results for Ant 3 in the WLAN 2.4 GHz band [Fig. 8(c)]. The radiation efficiency ranged from 41% to 66%, and the gain is between 0.7dBi∼1.3dBi. The second contribution frequency band of the same antenna was the WLAN 5G band, which had an efficiency of 33% to 78%, and the gain is between 1.1dBi∼3.7dBi. The results surpassed the commercial standard of >30%. As for Ant 4, efficiency in the GSM 850/900 band was between 54% and 66% [Fig. 8(d)], and the gain is between 0.8dBi∼1.2dBi. Efficiency in the other contribution frequency band (GPS) was 42% to 46%, and the gain is between 0.75dBi∼0.82dBi. Overall, the actual
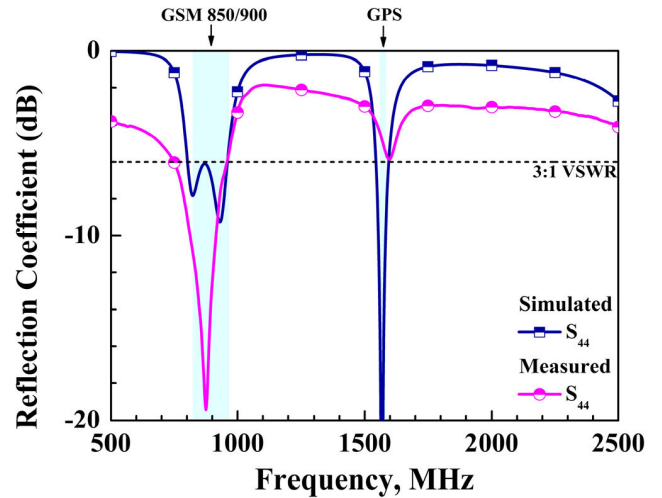
measured efficiency of each frequency band was relatively poor. Moreover, the trends in data changes were consistent, and the changes were ascribable to the differences in loss caused by welding during production.

B. PARAMETRIC ANALYSIS

We further examined the characteristics of the parasitic (Ant 1) monopole antenna with regard to the bandwidth ratio and impedance matching adjustment. We performed a parametric analysis of the end length of the parasitic monopole antenna. As displayed in Fig. 9(a), when the length S of the parasitic monopole antenna increased from 1.5 to 5.5 mm, the impedance matching and bandwidth ratio underwent varying changes. When S was 5.5 mm, because of the increase in the end path, the low-frequency L-slot mode had greater capacitance and the matching effect was poor. However, under the high-frequency mode, the shift in resonant frequency shift was reduced to 5100 MHz because of the increase in length. The gradual convergence of the parasitic monopole antenna mode and the slot mode produced an enhanced impedance matching effect. When S was 1.5 mm, the situation was reversed. Regarding the final parameter selection, an S of 3.5 mm was determined to yield the optimal impedance matching and bandwidth ratio. The antenna design principle of Ant 2 is the same as that of Ant 1; thus, the end length S of the parasitic monopole antenna of Ant 1 was used for parameter analysis. Furthermore, the characteristics of impedance matching adjustment and bandwidth ratio are discussed. The next step was to explore the effect of capacitance C_a on Ant 1. As presented in Fig. 10, the capacitor C_a was effective in adjusting the impedance matching of Ant 1 in the 5G FR1 n77/78/79 frequency band in the dual resonance mode. This explains the stable, favorable reflection coefficient of Ant 1 in this frequency band, as well as the satisfactory radiation efficiency. This design enabled Ant 1 to excite the 5G frequency band
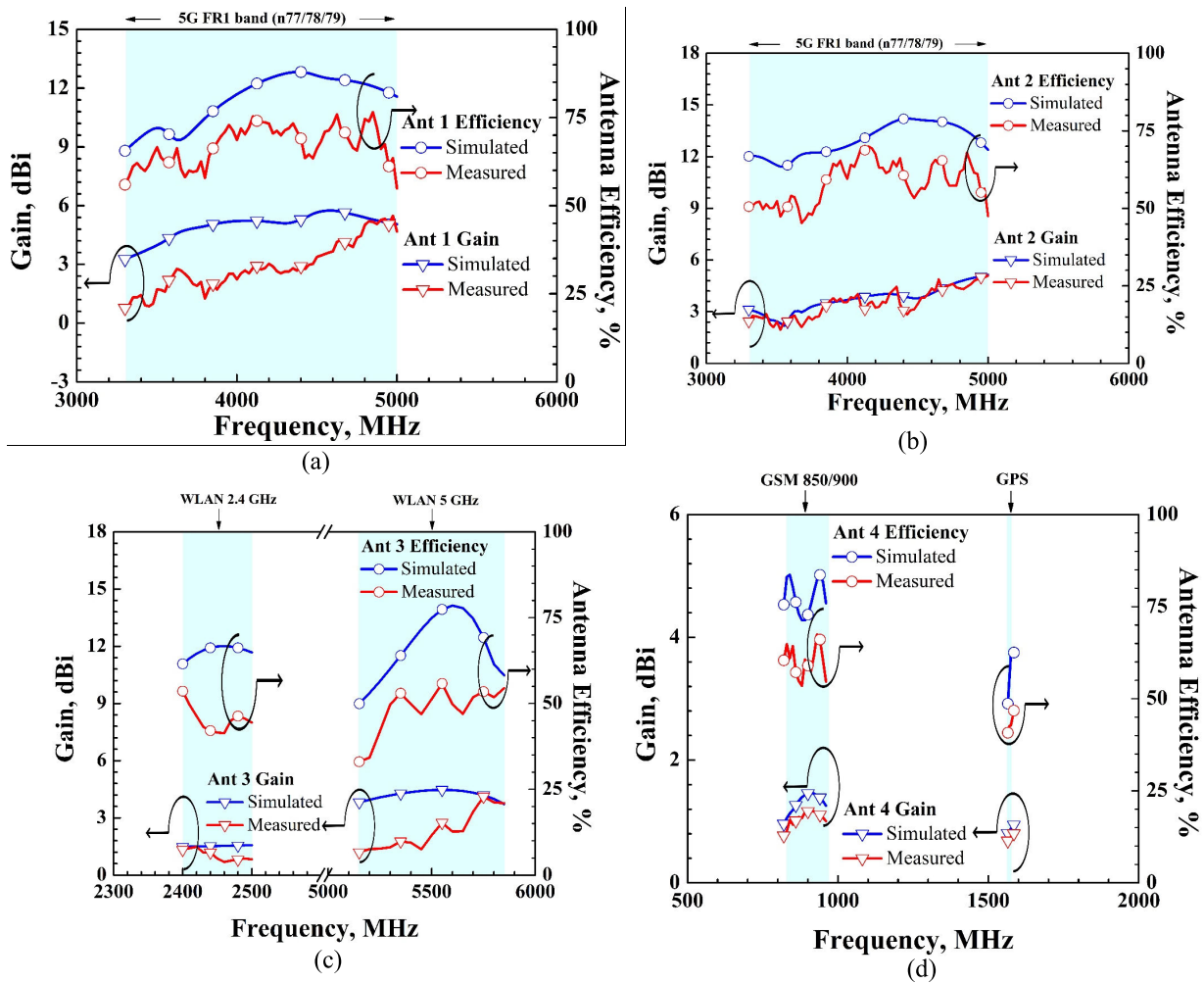
FIGURE 8. Simulated and measured efficiency and gain of (a) Ant 1 with the 5G FR1 n77/78/79 band, (b) Ant 2 with the 5G FR1 n77/78/79 band, (c) ANT 3 with the WLAN 2.4-GHz/5-GHz band, and (d) Ant 4 with the GSM 850/900 and GPS 1575 band.

with considerable adjustability. The multiple structures of ANT 3 are explained with regard to four parameters as follows. First is the analysis of the bending loop (point I to point K). The structure was disassembled into Ant 3a (without the bending loop) and Ant 3 (for the case of the proposed antenna). The status of Ant 3b (with a shorter bending loop) was also examined. Fig. 11(a) clearly indicates that Ant 3a only generated a coupled monopole (high-order mode) at 5400 MHz without a bending loop. This is not sufficient to cover the WLAN 5G band (5150–5850 MHz). A relatively short bending loop was added to Ant 3b to enable resonance at 5000 MHz. However, the resonant frequency of the coupled monopole (high-order mode) tended to increase. Therefore, the resonance length of the bending loop in Ant 3 (for the case of the proposed antenna) was increased. The resonant frequency was further reduced to 4550 MHz. Under this mode, the impedance matching of the loop antenna of one wavelength was adjusted. Fig. 11(b) indicates that the frequency band covers the WLAN 5G band (5150–890 MHz). Thus, the function of the structural part of the bending loop was defined to adjust the WLAN 5G band. At the same

time, we also optimized the slotted hole length of Ant 3. As shown in Fig. 12(b), the resonant frequency at the slot was approximately 3100 MHz. Increasing the length of the slotted hole L led to a downward trend in the resonant frequency of the half-wavelength loop antenna. This is because the slotted hole mode (3100 MHz) is similar in frequency to the fundamental mode of the coupled monopole (2450 MHz). Therefore, we can conclude that changing the length of the slot also affects the coupled monopole (basic mode). The analysis of these two parameters confirmed that the slot length L can independently control the mode of the WLAN 2.4-GHz band but does not substantially affect the WLAN 5-GHz band [Fig. 12(a)]. The design of the bending loop also allows for adjustment in the degree of modal matching in the WLAN 5-GHz band. Furthermore, the same independent characteristic does not affect the resonance mode of the WLAN 2.4-GHz band. These results demonstrate that the design of the WLAN dual-band (2.4-GHz/5-GHz) antenna can be flexibly adjusted. Subsequently, the band-pass filter was designed and analyzed. In Ant 3, a curved metal line segment connects point I to point J in order to couple it to
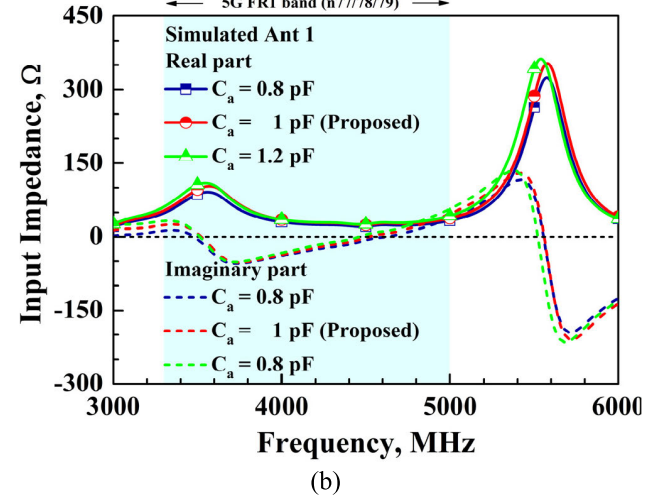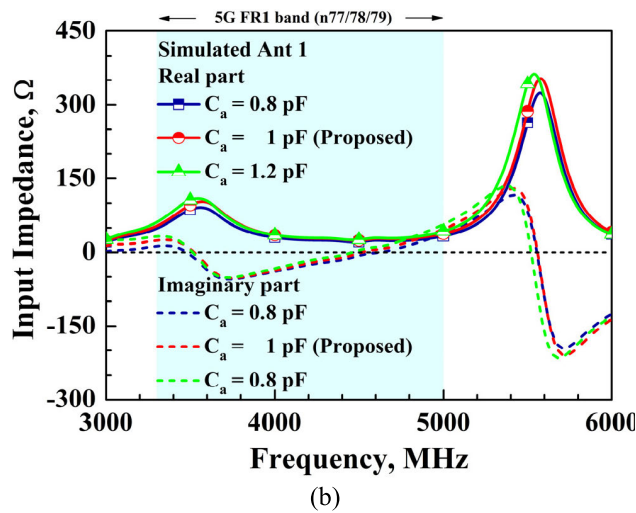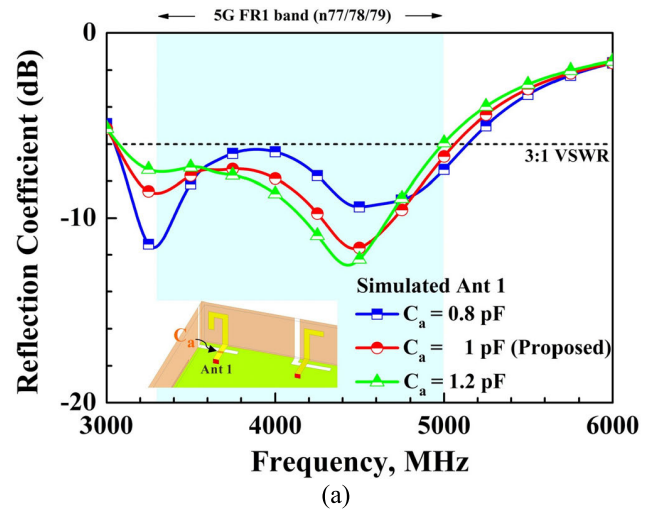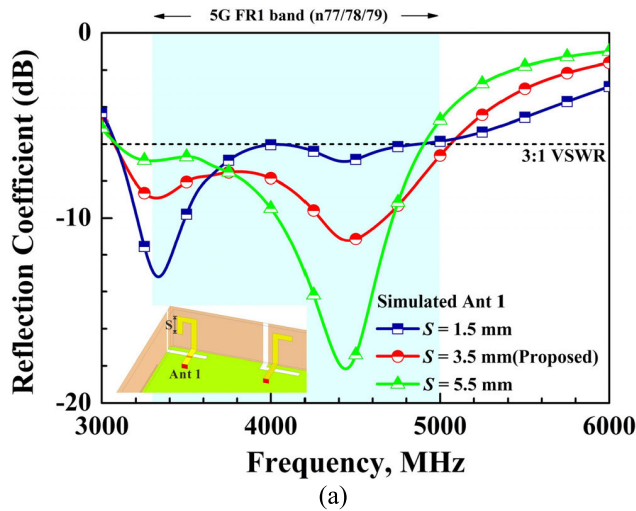
FIGURE 9. Comparison of (a) the reflection coefficient and (b) the input impedance of the parasitic monopole length S of Ant 1.

FIGURE 10. Comparison of (a) the reflection coefficient and (b) the input impedance of the variation in inductance C_a of Ant 1.

the metal frame. The fundamental mode and higher-order modes of the coupled monopole were resonated. A longer path was used to form a distributed inductance; subsequently, the lumped capacitance C_b was connected in series to form a band-pass filter. As presented in Fig. 13, the frequency bands that could be filtered from S_{3A} were either less than 2.3 GHz or ranged from 2.5 to 5.1 GHz. The filter function enabled the use of the WLAN 2.4-GHz and 5-GHz frequency bands. This design avoids the interference caused by other adjacent modal resonances. Part of the bending loop was used to adjust the impedance matching of the WLAN 5G band. For the sake of brevity, this is not discussed herein. Regarding Ant 4, we analyzed the dual resonance mode of the direct-fed metal frame and the dual open slot. Fig. 14 confirms that when the frame was coupled by the strip (corresponding to the Ant 4a state), resonance modes were generated at 820 MHz for the dual-slot mode and at 1900 MHz for the coupled metal frame mode. Regarding the direct-fed antenna in the metal frame (corresponding to the Ant 4b state), a usable resonance mode, namely the monopole mode, was generated

at 930 MHz. The end inductor L_a (corresponding to the Ant 4c state) was used to go to ground in order to form a high-pass filter matching circuit. Thus, the degree of impedance matching was successfully adjusted at 820 MHz for the dual-open-slot mode and at 930 MHz for the metal frame mode. The antenna with a dual-band band-pass filter design was further analyzed. The following three structures are discussed separately: Ant 4c (inductance L_a on terminal only), Ant 4d (a strip with inductance L_b), and Ant 4 (for the case of the proposed antenna). Fig. 15 shows the dual resonance mode of Ant 4c. During the analysis, the surface current distribution was examined. As presented in Fig. 16(a), the outer metal frame was in the monopole mode. Fig. 16(b) demonstrates the resonance of the GSM frequency band under the dual-slot mode. Next, consider the Ant 4d state (a strip with inductance L_b) to which a ground inductance L_b of 18 nH has been added. Part of the current on the metal frame was guided to the grounding surface [Fig. 16(c)]. The current flow on the metal frame thus formed a loop resonance path. The edge of the slot in the same area is shown in Fig. 16(d). From
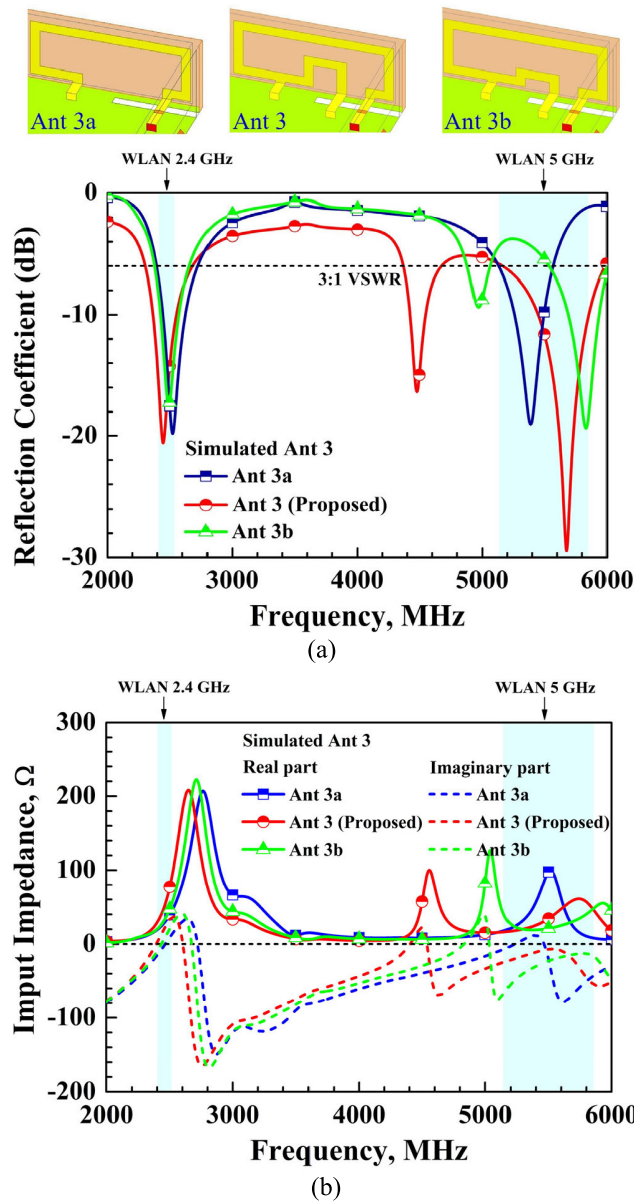
FIGURE 11. Simulated (a) reflection coefficient and (b) input impedance of Ant 3a (without bending loop), Ant 3 (for the proposed antenna), and Ant 3b (with a shorter bending loop).

FIGURE 12. Comparison of (a) the reflection coefficient and (b) the input impedance of the slot length L of Ant 3.

FIGURE 13. Simulation results of the band-pass filters of Ant 3. The embedded capacitor and distributed inductance series form were used.

another perspective, the dual-open-slot mode was resonanced at 820 MHz. On the metal frame, except for the coupling line segment, the surface current on the outer metal frame changes from M to O and then from point O to the ground inductance ($L_b = 18$ nH). The current starts at point N and flows along the edge of the slot. Fig. 16(e) indicates the formation of the 3D bending unipolar mode in which the metal frame and the slot coexist. Resonance is observable at 1250 MHz. The capacitor C_c was added to Ant 4 (the case of the proposed antenna). The frequency band impedance was adjusted; therefore, the original loop mode resonance path of Ant 4b, corresponding to Fig. 16(e), changed. The current path of the resonance mode is shown in Fig. 16(f), which corresponds to the monopole mode formed by the metal frame. Finally, the
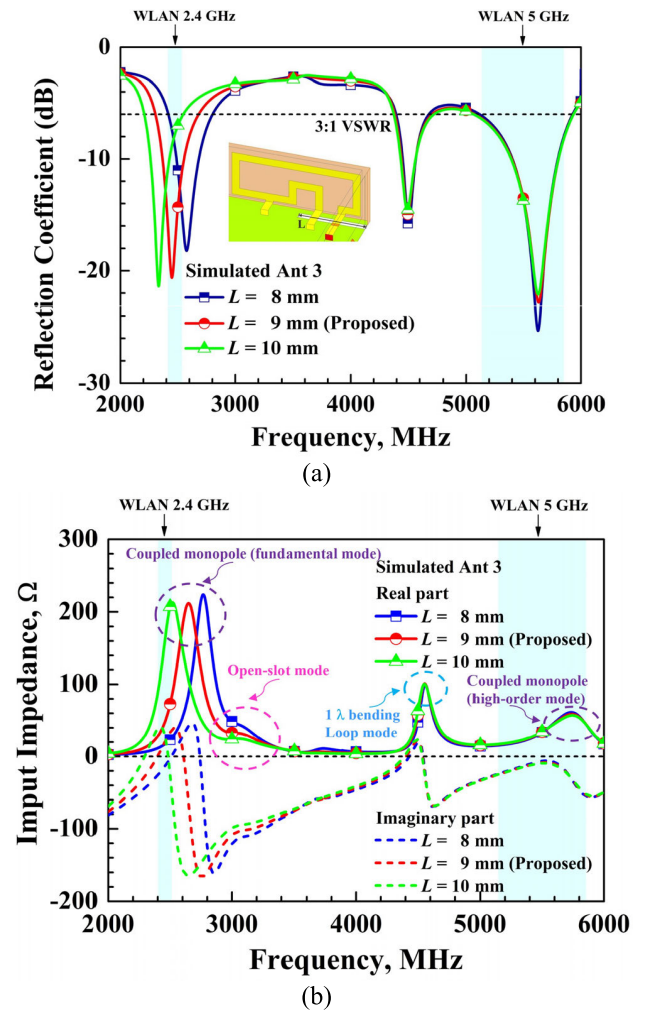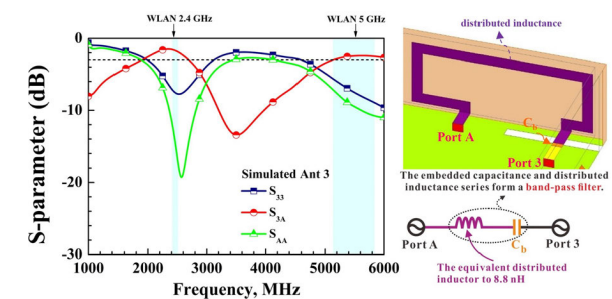
capacitor C_c was added in series with the inductance L_b to form a band rejection filter. The function enabled adjustments to impedance matching in the 3D bending monopole mode. Fig. 16(h) displays the current contributed to the GPS frequency band (1575 MHz). This concludes the discussion on the filter matching circuit. Fig. 17 indicates that when the capacitance C_c was increased, the three resonant frequencies in the GSM and GPS modes uniformly shifted to a lower frequency. This has a considerable impact on the GSM dual
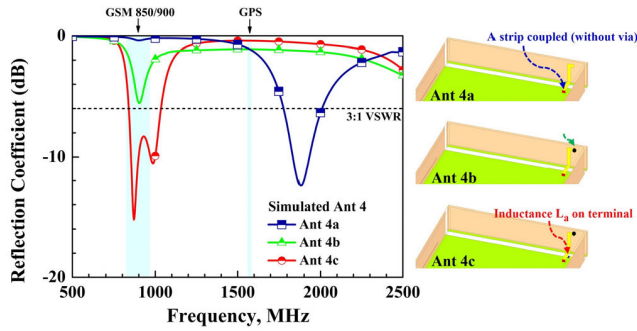
FIGURE 14. Simulated reflection coefficient of Ant 4a (a strip coupled to a dual open slot), Ant 4b (direct feed to the metal frame), and Ant 4c (inductance L_a on the terminal).
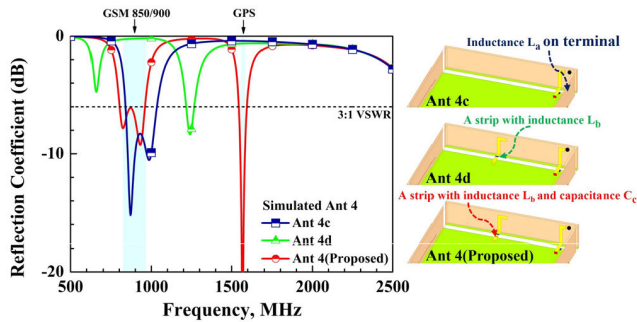

FIGURE 15. Simulated reflection coefficient of Ant 4c (inductance L_a on the terminal), Ant 4d (a strip with inductance L_b), and Ant 4 (for the proposed antenna).
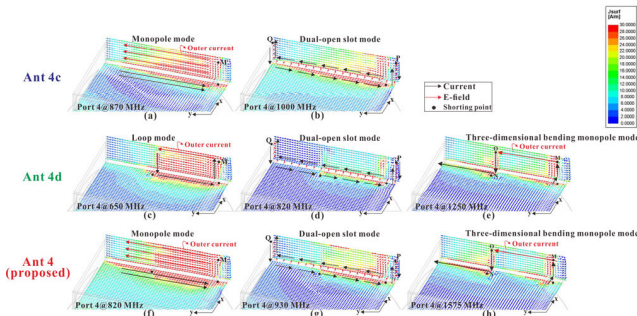

FIGURE 16. Simulated vector current distributions of Ant 4. Ant 4c is excited (a) at 0.87 GHz in the monopole mode and (b) at 1 GHz in the dual-open-slot mode; Ant 4d is excited (c) at 0.65 GHz in the loop mode, (d) at 0.82 GHz in the dual-open-slot mode, and (e) at 1.25 GHz in the 3D bending monopole mode; Ant 4 is excited (f) at 0.82 GHz in the monopole mode, (g) at 0.93 GHz in the dual-open-slot mode, and (h) at 1.575 GHz in the 3D bending monopole mode.

resonance mode, mainly attributable to the increase in the capacity of the capacitive impedance at low frequencies—that is, the path of the resonance current to the ground plane. In Fig. 18, when L_b was increased, the GPS band resonance mode shifted to a low frequency, whereas the GSM dual resonance mode gradually converged. Notably, the changes in C_c and L_b were all due to the modalities of the three resonance paths (i.e., metal frame current, dual open-slot, and 3D bending monopole) with regard to the passage of currents from point O to point N. This further leads to changes in the resonant frequencies of the three modes. The band-stop filter in Ant 4 is discussed and analyzed as follows.
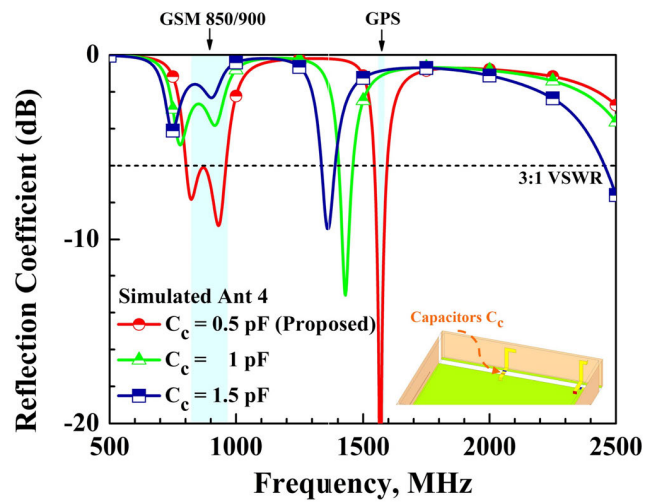

FIGURE 17. Comparison of reflection coefficients for variations in capacitance C_c in Ant 4.

The frequency response in Fig. 19 was examined and S_{45} was analyzed. The frequency response exerted a dual-band (center frequencies of 0.68 and 1.22 GHz) band-stop filter effect, with the frequency range of GSM 850/900 filtered out. In the final state (Fig. 20), a lumped capacitor C_c was added and a lumped inductor L_b was connected in series to form a band-stop filter. The analysis of S_{45} in Fig. 20 revealed that all three frequency bands functioned as approximate band-stop filters (center frequencies of 0.9 and 1.575 GHz). In sum, this band-stop filter affected the resonance modes of the GSM 850/900 and GPS frequency bands (1575 GHz). At the same time, favorable antenna performance was achieved.

IV. MIMO CHARACTERISTIC AND HAND TISSUE DISCUSSION

The application of an 5G FR1 band in a 2×2 MIMO antenna setting is the future trend for 5G smart watches. The premise is to employ a 5G FR1 n77/78/79 band and a 2×2 antenna design in a small space within a smart watch. The impact of the metal body must be considered in the design process. Achieving favorable MIMO antenna performance is a major challenge in this regard.

A. DIVERSITY PERFORMANCE AND CHANNEL CAPACITY

The proposed antennas utilize the gaps of the metal frame. The function of the slot antenna (Ant 1) was realized through proper excitation. Field diversity with regard to the angle of the main beam direction was achieved in the proposed antenna because of the characteristics of the slot antenna on the frame (Ant 2). This is because of the physical direction of the opening of the slot antennas in Ant 1 and Ant 2. As shown in Fig. 21, the E_θ (Phi) of Ant 1 on the XY plane was $-80°$, and the E_θ (Phi) of Ant 2 was $106°$. Moreover, the distance between Ant 1 and Ant 2 was only 14.5 mm (0.13 λ_0). Even without the addition of decoupling components to the design, the isolation performance still met the commercial application standard (less than -10 dB).
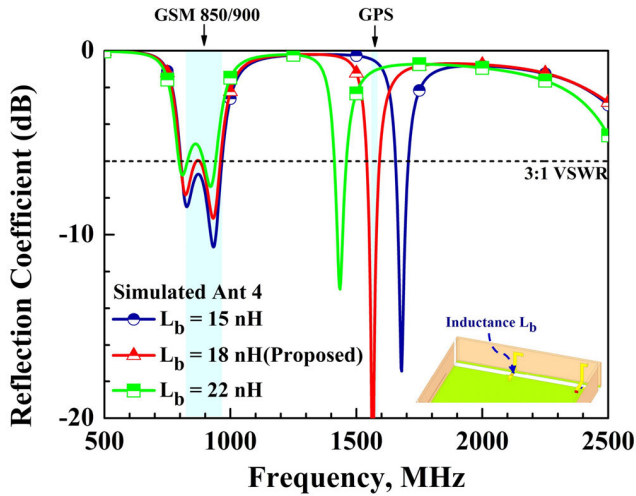
FIGURE 18. Comparison of reflection coefficients for variations in inductance L_b in Ant 4.
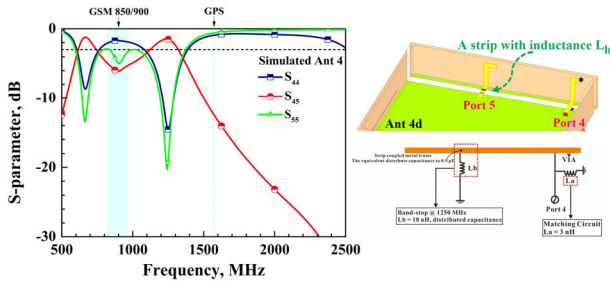

FIGURE 19. Simulation results of band-stop filters of Ant 3. The embedded capacitor and embedded inductance series form were used.
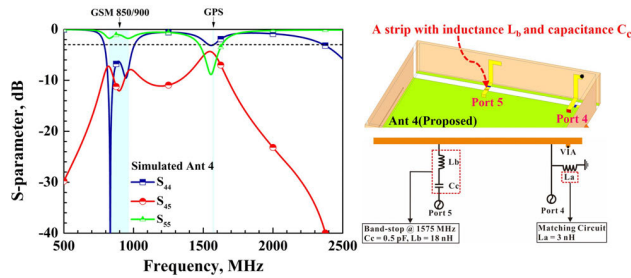

FIGURE 20. Simulation results of band-stop filters of Ant 3. The embedded capacitor and embedded inductance series form were used.

In general, the diversity effect between antenna arrays yields lower envelope correlation coefficients [40], [41], as indicated in equation (2). Both the radiation field size and the spatial direction angle of the two antennas must be considered in the calculation.

$$\rho_e \text{ (ECC)} = \frac{\left| \int_{4\pi}^{\int} \left[\vec{E}_1 \left(\theta,_A \phi \right) \cdot \vec{E}_2 \left(\theta,_A \phi \right) \right] d\Omega \right|}{\int_{4\pi}^{\int} \left| \vec{E}_1 \left(\theta,_A \phi \right) \right|^2 d\Omega \int_{4\pi}^{\int} \left| \vec{E}_2 \left(\theta,_A \phi \right) \right|^2 d\Omega} \quad (2)$$

$$DG = 10\sqrt{1 - (ECC)^2} \quad (3)$$

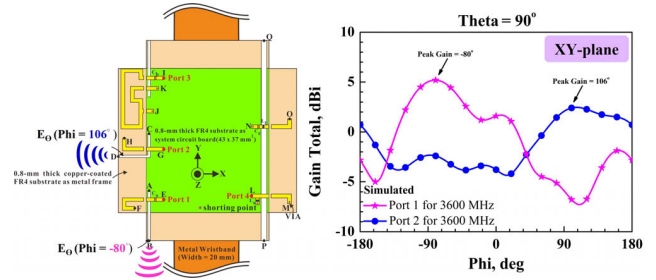$$\eta_{\text{MUX}} = \sqrt{(1 - |\rho|^2)\eta_1 \eta_2} \quad (4)$$

FIGURE 21. Simulation of Ant 1 and Ant 2 for the 3.6-GHz radiation field (gain total) in the Cartesian coordinate system.

Another critical parameter for evaluating the degree of antenna diversity performance is diversity gain (DG) [42]. As indicated in equation (3), the ECC results directly affect the DG results. DG is in the optimal state when ECC = 0, indicating the absence of mutual interference between the antennas. This situation produces a DG of 10 dB. The interference between the corresponding antennas is the most severe when DG = 0 dB (ECC = 1). On this basis, the ECC and DG of the proposed antenna are combined in Fig. 22(a). Whether simulated or measured, the ECC performance of the proposed antenna is below 0.1, considerably lower than the commercial application standard (ECC = 0.5). In the 5G FR1 band, the DG is also above 9.97, confirming that the diversity effect between MIMO antennas is excellent. Furthermore, the peak gain and multiplexing efficiency in two scenarios (with and without metal straps) were evaluated. Multiplexing efficiency [43] is defined in equation (4), where the gains of the two MIMO antennas are expressed as η_1 and η_2, respectively, and where ρ represents the complex envelope correlation coefficient between the two antennas. Moreover, ρ can be approximated to $|ECC|^2$. The optimal theoretical state is achieved when the efficiency of both antennas is 100% and they do not affect each other at all (ECC = 0). In this situation, η_{MUX} equals 0 dB. However, achieving the ideal state in practical applications is impossible. In the design of wearable device antennas, the commercial application standard requires the antenna efficiency to exceed 30% and the ECC to be less than 0.5. This standard calculation corresponds to a η_{MUX} of -5.85 dB. As presented in Fig. 22(b), in the scenario without a metal strap, the peak gain was approximately equal to $2-5$ dBi. The peak gain of the proposed antenna in the scenario with a metal strap was higher: $3-5.8$ dBi. This phenomenon indicates that the metal strap has a positive effect on the antenna gain. A detailed discussion on these results is presented in the following section. Data on the performance of the proposed antenna were comprehensively examined to obtain the multiplexing efficiency, the results of which were all above -2dB, higher than the commercial application standard. Finally, the ECC of the MIMO antenna was substituted into equation (5) to calculate the channel capacity. In the equation, ρ_{12} was considered with regard to the radiation field of the two antennas on the basis of the spherical coordinate system.

Equation 6 contains the efficiency (a%, b%) of Ant 1 and Ant 2. In the calculation, Rayleigh fading was used as the standard [43], and the reflection interference and influence of numerous of scattered signals in the space were taken into account, including the maximum and minimum attenuation. The channel capacity was computed by averaging 10,000 Rayleigh fading realizations, and the signal-to-noise ratio was 20 dB. As shown in Fig. 23, the channel capacity of the 2 × 2 MIMO array was approximately 8.8 bps/Hz. According to the optimal theoretical rate (11.5 bps/Hz) [44], the transmission rate of channel capacity reached 76.5%, in line with the requirements of 5G communications and IoT applications.

$$C = \log_2 \begin{vmatrix} 1 + SNR \cdot a\% & SNR \cdot \rho_{12} \cdot b\% \\ SNR \cdot \rho_{21}^* \cdot a\% & 1 + SNR \cdot b\% \end{vmatrix} \quad (5)$$

In short, the proposed antenna performed well when used in a 5G FR1 band within a 2 × 2 MIMO configuration. The radiation pattern is displayed in Fig. 24; the loop-shaped line segment in Ant 3 is coupled to the metal frame. The field pattern effectively radiates toward the exterior of the device (corresponding to the −X direction). This design helps reduce the specific absorption rate (SAR) and shortens the resonance path. By using the length of the L-shaped slot, the impedance matching of the WLAN 2.4-GHz/5-GHz frequency band can be adjusted at the same time.

B. HAND TISSUE AND SAR EVALUATION

Fig. 25(a) presents the scenario where the proposed antenna is placed on a simulated wrist model composed of skin, fat, muscle, and bone. The thicknesses of these components in human tissue structure are 0.65, 4.55, 1.3, and 26 mm, respectively, and the distance between the antenna and the wrist model is 2 mm. Fig. 25(b) displays the side view of the proposed antenna on the wrist model. The radiation efficiencies of the 5G FR1 n77/78/79 band, WLAN 2.4-GHz/5-GHz band, GSM 850/900, and GPS frequency bands in free space and in the hands-on state were compared. The center frequency of each frequency band was taken as the setting of the dielectric coefficient and the conductivity of the skin, fat, muscle, and bone [45], [46], as shown in Table 2. These subitem settings ensured the independent accuracy of the simulation of each resonant frequency band.

TABLE 2. Relative permittivity and conductivity in wrist tissue.

Wrist tissue	ϵ_r				σ (S/m)			
	[1]1.2 GHz	[2]2.45GHz	[3]4GHz	[4]5.5GHz	[1]1.2 GHz	[2]2.45GHz	[3]4GHz	[4]5.5GHz
Bone	[1]20.2	[2]18.5	[3]16.9	[4]15.6	[1]0.41	[2]0.8	[3]1.39	[4]2.05
Fat	[1]5.4	[2]5.3	[3]5.1	[4]4.9	[1]0.05	[2]0.11	[3]0.18	[4]0.27
Skin	[1]40.2	[2]38	[3]36.5	[4]35.3	[1]0.96	[2]1.46	[3]2.34	[4]3.46
Muscle	[1]54.4	[2]52.7	[3]50.8	[4]48.8	[1]1.05	[2]1.74	[3]3.01	[4]4.6

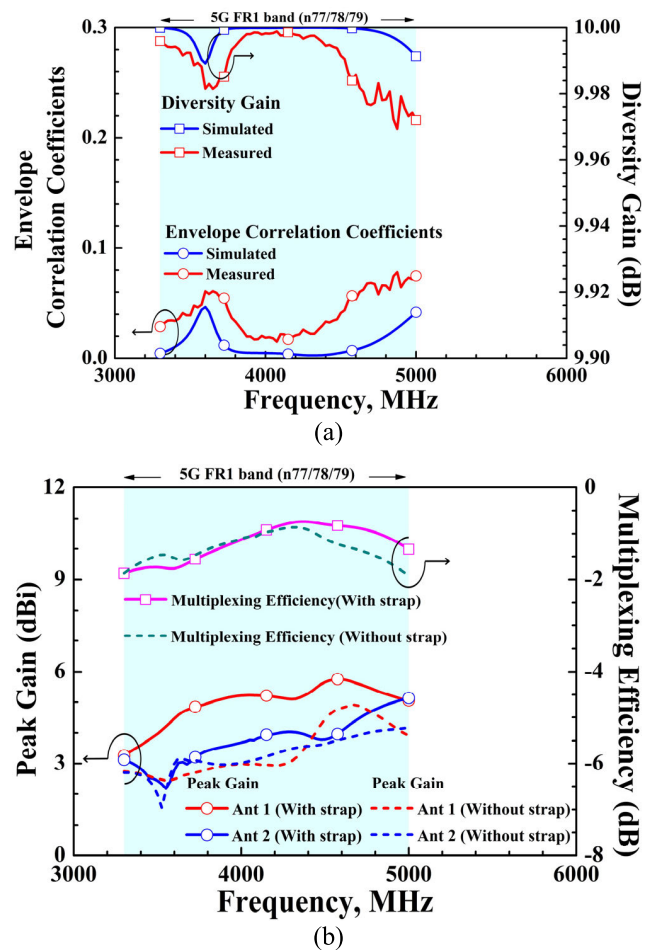**FIGURE 22.** Calculated MIMO parameters in the 5G FR1 n77/78/79 band of Ant1 and Ant 2. (a) ECC and diversity gain and (b) peak gain and multiplexing fficiency.
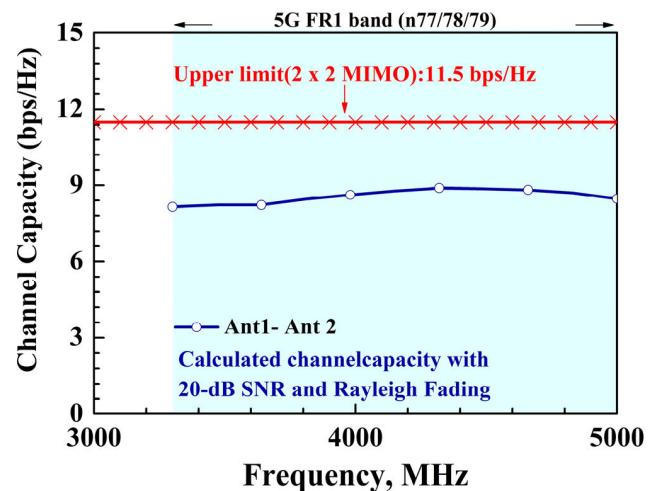

FIGURE 23. Calculated channel capacity from the measured results.

We first introduced the design principle for combining the antenna with a metal strap. The metal strip can be regarded as an extension of the ground plane (−Z direction), affecting
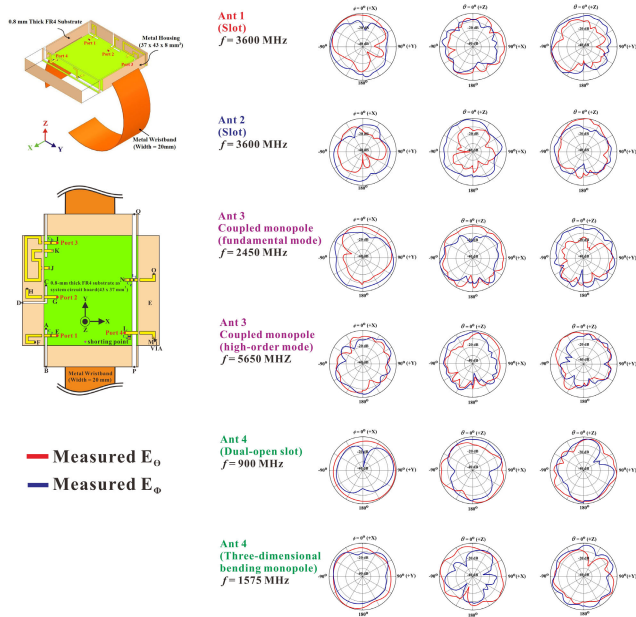
FIGURE 24. 2D radiation patterns of the four antennas.

TABLE 3. Proposed antenna system with the addition of a metal strap.

Proposed antenna with metal wristband					
	Antenna Type	**Operation Band**	**Gain (dBi)**	**Directivity (dBi)**	**Efficiency (%)**
Ant 1	Open slot	5G FR1 Band (n77/78/79)	3.2 ~ 5.7	5.2 ~ 6.6	62 ~ 80
Ant 2	Open slot	5G FR1 Band (n77/78/79)	2.0 ~ 4.1	3.8 ~ 4.8	66 ~ 88
Current phase of ground plane					

the current direction of the ground plane. After the metal strap was added, the current phase of the ground plane was in the dipole mode direction (Table 3). The radiation pattern of Ant 1 in Fig. 26 shows that the radiation pattern is a null point in the ±Z direction. The L-slot resonance mode radiates in the −Y direction, and the superposition of far-field energy

TABLE 4. Proposed antenna system without the addition of a metal strap.

Proposed antenna without metal wristband					
	Antenna Type	**Operation Band**	**Gain (dBi)**	**Directivity (dBi)**	**Efficiency (%)**
Ant 1	Open slot	5G FR1 Band (n77/78/79)	2.3 ~ 4.7	4.7 ~ 6.0	57 ~ 74
Ant 2	Open slot	5G FR1 Band (n77/78/79)	1.8 ~ 3.8	3.8 ~ 4.4	62 ~ 78
Current phase of ground plane					

increases the gain and directivity of the radiation field in this direction. In the condition without the metal strap, the vector current distribution on the grounding surface flowed in the form of a loop antenna mode, helping the field pattern more closely resemble omnidirectional radiation (Table 4). Tables 3 and 4 present the gain and directivity in the presence and absence, respectively, of metal straps. The radiation efficiency was almost the same in these two conditions. When a metal strap was considered in the proposed antenna system, gain and radiation were higher, and a zero point was generated in the −Z direction (corresponding to the wrist position). The results indicate that this design can reduce the gradual decline over time in the radiation efficiency of the antenna when placed in a wearable device, a phenomenon attributable to the loss in electromagnetic energy caused by proximity to the human body. Part of the energy that the antenna radiates is absorbed by the human body and converted into heat. Therefore, the radiation efficiency of the antenna is reduced. After the optimization of the radiation field pattern, owing to the addition of metal strips, the radiation efficiency of the antenna can be enhanced. Table 5 presents the efficiency of the proposed antenna system in free space and on the wrist model. As mentioned, a favorable radiation efficiency of >25% in each working frequency band of Ant 1–Ant 4 was achieved. As shown in Fig. 27, the radiation efficiency met commercial standards. Although the radiation field pattern of Ant 2 was affected by the metal strap, directivity was retained.

TABLE 5. Simulated efficiency of the proposed antenna system in free space and on the wrist model.

Proposed Antenna	Free space Efficiency (%)	On wrist Efficiency (%)
Ant 1 (3300 ~ 5000 MHz)	63 ~ 79	47 ~ 62
Ant 2 (3300 ~ 5000 MHz)	61 ~ 87	25 ~ 39
Ant 3 (2400 ~ 2500 MHz)	61 ~ 68	35 ~ 41
Ant 3 (5150 ~ 5850 MHz)	48 ~ 80	39 ~ 62
Ant 4 (820 ~ 960 MHz)	71 ~ 83	27 ~ 30
Ant 4 (1565 ~ 1585 MHz)	48 ~ 62	28 ~ 36

However, this radiation was mainly concentrated in the −X direction (toward the fingers). Therefore, the radiation efficiency was reduced. By contrast, Ant 4 had a lower frequency band than the other antennas, and the radiation pattern was omnidirectional. Therefore, its performance on the wrist model was substantially poorer, resulting in a sharp decline in the radiation efficiency in the hands-on condition. Fig. 26 displays the radiation field pattern in the presence and absence of a metal strap. When a metal strap was added to the proposed antenna system, we observed that the radiation field pattern exhibited directivity and that the energy radiating in the direction of the wrist (−Z direction) was reduced. This design can be effective in improving both the radiation efficiency of hands-on use and the battery life of the smart watch. The SAR, a measure of the electromagnetic energy absorbed by the human body, is expressed as the unit mass of the dielectric and represents the relationships between electric field strength, conductivity, mass density, and absorption rate as follows:

$$\text{SAR} = \frac{\sigma |E|^2}{\rho} \tag{6}$$

where E is the strength of the electric field in the tissue (V/m) and σ and ρ are the conductivity (S/m) and mass density (kg/m^3) in the tissue, respectively. To simulate the effect of the proposed antenna system on human wrist tissue, we imported the wrist model into simulation software (CST Studio Suite) to analyze the SAR value [47]. The 5G FR1 n77/78/79 band, 5G FR1 n77/78/79 band, WLAN 2.4-GHz/5-GHz band, and GSM 850/900 plus GPS band corresponded to ports 1, 2, 3, and 4, respectively. To ensure the safety of the wearer of such devices, the US Federal Communications Commission—the relevant regulatory authority—has SAR standards. On this basis, the SAR was set according to the IEEE C95.1-2005 standard [2]. The SAR was assessed on a wrist manikin [6]. The SAR values corresponding to all resonance modes after antenna excitation are displayed in Table 6. Fig. 28 presents a scenario where
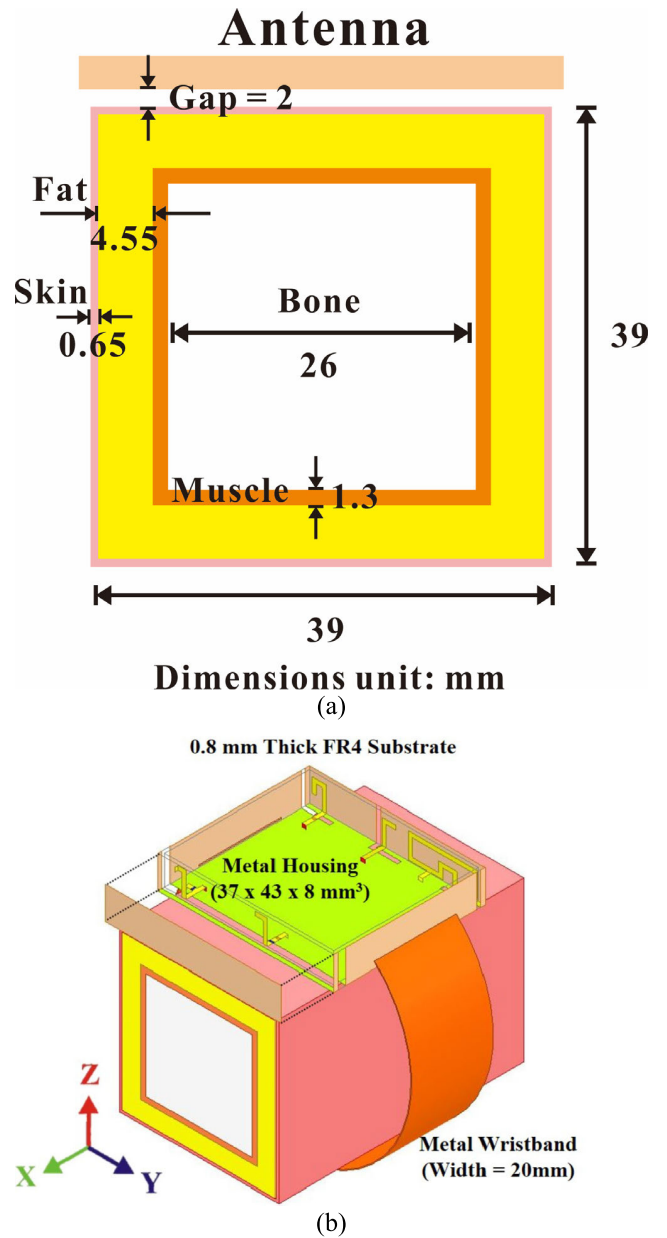
FIGURE 25. Simulation of the proposed antenna system in the wrist model: (a) multilayer representation and (b) side view of the proposed antenna on the wrist model.

the antenna system and the wrist tissue were 2 mm apart. The distribution of SAR values excited by Ant 1 at 3.6 GHz was mainly concentrated in the −Z and −Y directions, corresponding to the skin and fat layers of human wrist tissue. This is because the L-slot in the antenna design caused the current to be predominantly concentrated in the ground plane and the slotted hole. As indicated in Fig. 29, when Ant 2 was excited at 3.6 GHz, the SAR was concentrated on both sides of +y and −y. Ant 2, an L-slot antenna, was designed to be in the middle of the substrate. Therefore, the current excited by the antenna flowed in the +y and −y directions. The loop-shaped curved metal strips in the Ant 3 setup allowed for coupling with the metal frame during excitation. Radiation

FIGURE 26. Radiation pattern of the proposed antenna system (a) with and (b) without a metal strap.

FIGURE 27. Efficiency of the proposed antenna system in free space and in the wrist model.

TABLE 6. Sar values when the antenna system and wrist tissue were 2 mm apart.
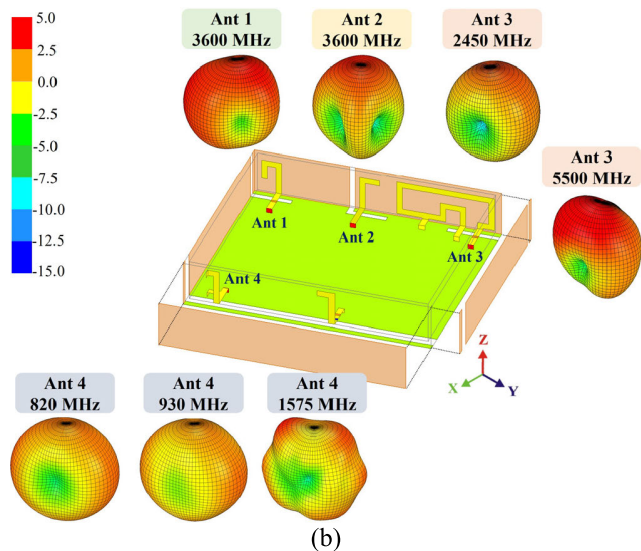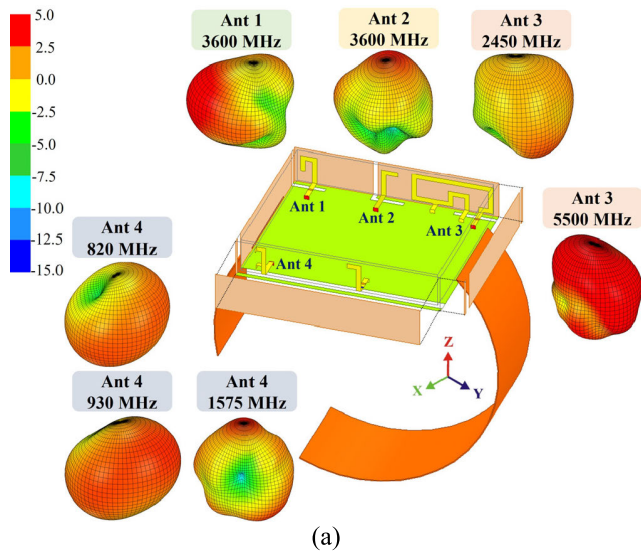
Proposed Antenna Port	Operation Bands	Operation Frequency (MHz)	10-g SAR (W/kg)	1-g SAR (W/kg)
Port 1 with wrist tissue	(1) 5G FR1 Band (n77/78/79)	3600	0.67	1.08
Port 1 with wrist tissue	(1) 5G FR1 Band (n77/78/79)	4400	0.64	1.01
Port 2 with wrist tissue	(1) 5G FR1 Band (n77/78/79)	3600	0.98	1.21
Port 2 with wrist tissue	(1) 5G FR1 Band (n77/78/79)	4400	1.21	1.54
Port 3 with wrist tissue	(2) WLAN 2.4G	2450	0.49	0.93
Port 3 with wrist tissue	(3) WLAN 5G	5500	0.41	0.84
Port 4 with wrist tissue	(4) GSM 850/900	820	0.25	0.788
Port 4 with wrist tissue	(4) GSM 850/900	930	0.54	1.05
Port 4 with wrist tissue	(5) GPS	1575	0.26	0.58

Operation Frequency Bands:
(1) 5G FR1 Band n77/78/79(3300 MHz~5000 MHz),
(2) WLAN 2.4G(2400 MHz~2500 MHz),
(3) WLAN 5G(5150 MHz~5850 MHz),
(4) GSM 850/900(824 MHz~960 MHz),
(5) GPS(1575 MHz)

FCC limitation : 10-g SAR 4.0(W/kg) /1-g SAR 1.6(W/kg)

was designed to follow the −x direction. Fig. 30 displays the same result. When Ant 3 was excited at 2.45 and 5.65 GHz, the SAR values were all distributed in the −x direction. In Ant 4, the current at the open slot (corresponding to the −Y direction) was relatively strong. The SAR values (0.82, 0.93, and 1.575 GHz) were all concentrated in the −y direction (Fig. 31). We confirmed that the SAR value of the proposed antenna system was less than the corresponding 10-g SAR limit value of 4 W and the 1-g SAR limit value of 1.6 W set by the US Federal Communications Commission. Our results confirm that the proposed antenna system was effective in making the radiation field directional and in reducing the radiation in the wrist direction (i.e., −Z) after the metal strap was added. In the wrist model, a favorable radiation efficiency exceeding 25% was maintained, effectively increasing the battery life of the wearable device and reducing the radiation impact of the antenna on human wrist tissue.
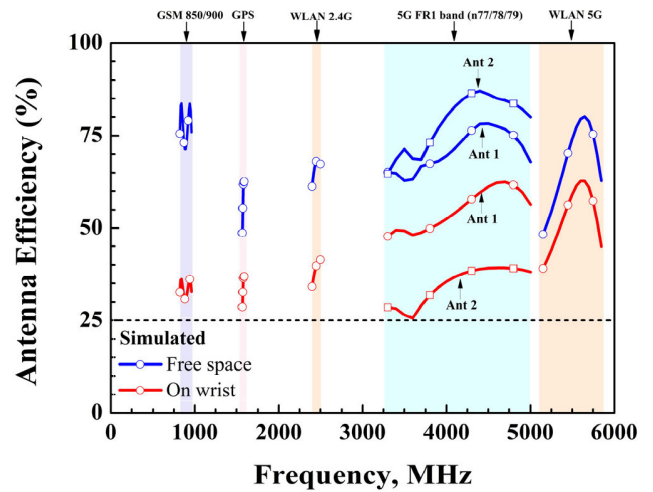
C. COMPARATIVE REVIEW OF ANTENNAS IN SMART DEVICES

This section reviews studies on built-in antennas in smart wearable devices. Table 7 lists the types of wearable antennas using various frequency bands. One antenna design was effective in reducing radiation in the direction of the wrist, but the antenna system occupied the entire loop area of the watch device in a single frequency band [1]. In [2], after the metal appearance was examined, the overall frame was
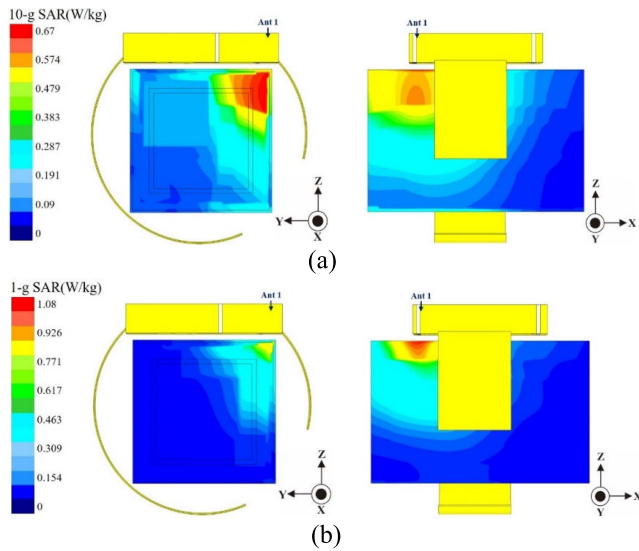
FIGURE 28. SAR distributions for Ant 1 excited at 3.6 GHz when the antenna system and wrist tissue were 2 mm apart visualized using CST software under the following conditions: (a)10-g SAR and (b) 1-g SAR.

FIGURE 29. SAR distributions for Ant 2 excited at 3.6 GHz when the antenna system and wrist tissue were 2 mm apart visualized using CST software under the following conditions: (a) 10-g SAR and (b) 1-g SAR.

FIGURE 30. SAR distributions for Ant 3 excited at 2.45 and 5.5 GHz when the antenna system and wrist tissue were 2 mm apart visualized in CST software under the following conditions: (a)10-g SAR and (b) 1-g SAR under excitation at 2.45 GHz and (c)10-g SAR and (d) 1-g SAR under excitation at 5.65 GHz.

directly used to achieve loop-antenna-type resonance. A high-order resonance mode was also employed. Duan and Xu discussed an antenna with an umbrella-shaped monopole for device implantation in medicine and telemetry [3]. Wu *et al.* investigated an internal shorted monopole providing a wide bandwidth for Bluetooth operations in the 2.4-GHz band [4]. In one study, a scenario involving a completely metallic case and strap was considered. Designed with a single frequency band (2.4 GHz under Wi-Fi), the metal surface area of the watch was $\pi \times 23 \times 10$ mm3. A circular slot antenna with an arc length of 97 mm was used [5]. In another study, the antenna system was designed according to the diameter of the device, limiting flexibility in adjustment in commercial

use [6]. In [7], the resonant frequency and matching were determined by the overall watch diameter, and the energy radiated by the antenna was focused in the direction of the wrist. A few investigations have employed MIMO arrays for BT/Wi-Fi bands and assessed pattern diversity performance [6], [7]. Multifrequency resonance was achieved after shared slots and shared radiators were used to resolve the problem of the metal appearance. However, the MIMO array and the SAR evaluation in the context of 5G applications were not considered [8]. In [9], the upper layer of the device had an LDS frame with a relative permittivity of 2.92, whereas the lower layer was an IFA antenna with a nonmetallic frame. In a study by Xu and Duan, resonance in the overall metal strap and ground plane was achieved in LTE (700 and 1.7–2.7 GHz) [10]. Since 2015, 4G frequency bands and LTE

FIGURE 31. SAR distributions for Ant 4 excited at 0.82, 0.93, and 1.575 GHz when the antenna system and wrist tissue were 2 mm apart visualized using CST software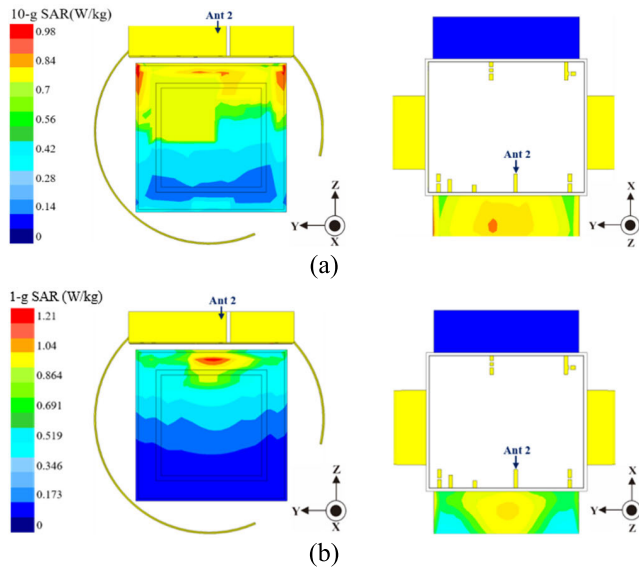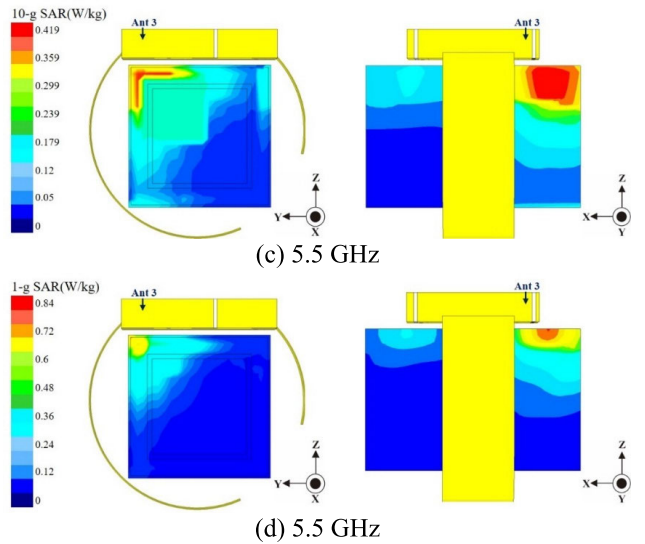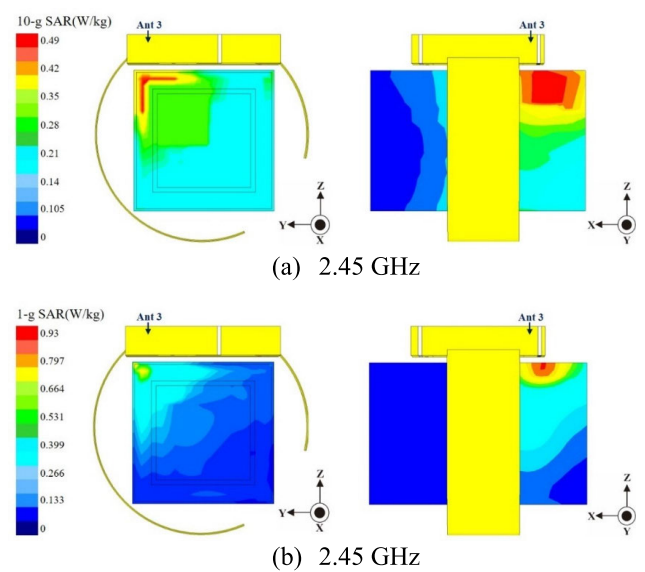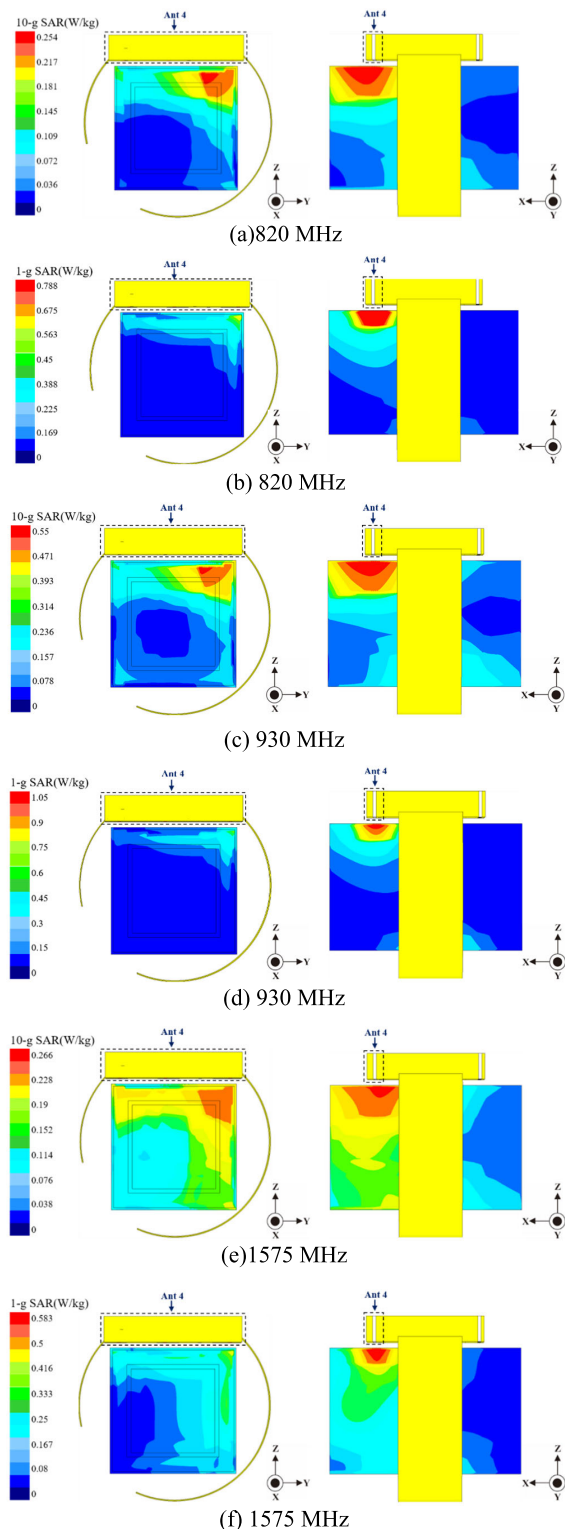 under the following conditions: (a)10-g SAR and (b) 1-g SAR under excitation at 0.82 GHz; (c)10-g SAR and (d) 1-g SAR under excitation at 0.93 GHz; and (e)10-g SAR and (f) 1-g SAR under excitation at 1.575 GHz.

frequency bands have gradually been adopted in wearable devices. In recent years, LTE, GPS, and Wi-Fi 2.4-GHz

bands have also been integrated into smart devices [10]. A cuboid wrist model measuring $70 \times 50 \times 40$ mm3 was used in another relevant investigation [24]. The design achieved bandwidth enhancement and was applied in biomedical monitoring [25]. Hamouda *et al.* reported on a spiral-shaped planar inverted-F antenna for use in a medical implant communication service [26]. Sojuyigbe and Daniel used a PCB-integrated antenna and evaluated the effect of metal shielding on antenna performance in smart watches [27]. A similar design concept involved the application of a loop antenna into a metal frame in smart watches employing GPS, Bluetooth, and Wi-Fi technology [16]. The millimeter-wave frequency band was designed for the configuration of 2×2 MIMO arrays and the evaluation of SAR [28]. Circularly polarized antennas [29] and semiflexible antennas [30] have been proposed for biomedical applications. Antennas using the Wi-Fi 2.4-GHz band or Wi-Fi 5-GHz band have been common in studies published over the past year [31], [32]. A textile antenna featuring a patch with a C-shape etching slot was proposed for Wi-MAX applications [33]. Moreover, IoT applications involving wireless charging have been proposed for integrated circuits [34]. Others have suggested designing a dual circular patch [35] or a wearable antenna with a resettable frequency band [36] for human tissue sensing and biomedical applications. Dang proposed employing shorting strategies in textile applications, specifically in buttons on clothing [37]. Recently, the incorporation of radiofrequency identification technology into wearable systems [38] was considered, as was the dual coverage of the Wi-Fi 2.4-GHz band and the 5G m77 band (3.4–3.6 GHz) for off-body communication [39]. Table 7 presents a comparison of studies with regard to several indicators. Numerous studies on wearable devices have investigated the influence of wrist models on antenna performance [1], [8], [25], [27]–[31], [35]. In most studies, designs were specific to a single frequency band [1]–[7], [24], [28]–[32], [34], [35], [38]. However, shortcomings remain in the comparison of various indicators. With the development of the IoT, connections through 5G communications technology are becoming increasingly ubiquitous. The design and performance of antennas in wearable devices, as well as the frequency bands used, must keep pace with these technological advances. The achievement of field diversity in a small space supports a multiantenna MIMO configuration. A critical consideration is whether each frequency band meets international standards under the addition of a wrist model. In this study, the low-attenuation-specific GSM 850/900 band and NB-IoT band 8 were employed. Furthermore, we designed an antenna utilizing the GPS (1575 MHz) band for IoT and RTLS scenarios. Notably, the 5G FR1 n77/n78/n79 band was configured as a 2×2 MIMO array, and a diversity function was realized. Examination of the results presented in the literature indicates that the wearable device antenna can be combined with a metal frame and a metal strap, covering not only the common WLAN 2.4/5G frequency band but also narrowband IoT band 8 and GSM, GPS, and 5G

TABLE 7. Performance comparison of Wearable antennas.

Ref.	Antennas type /Metal frame / Metal belt	Operation frequency bands	Dimensions (mm³)	Pattern diversity	MIMO	Optimization design on hand	Scope of application	SAR evaluation
[1]	Annular Slot / Yes/ No	①Wi-Fi 2.4G	21²*π*10	No	No	Yes	BT/WIFI applications	Yes
[2]	Loop antenna into metal frame/Yes /No	①Wi-Fi 2.4G	50*40*5	Yes	Yes	No	BT/WIFI applications	No
[3]	Wristband antenna with mbrella-shaped monopole/Yes /No	①Wi-Fi 2.4G	60*30*60	No	No	No	4G LTE	No
[4]	shorted monopole / No /No	①Wi-Fi 2.4G	37*37*10	No	No	No	4G LTE	No
[5]	Slot antenna /Yes / No	①Wi-Fi 2.4G	23*23*π	Yes	Yes	No	BT/WIFI applications	No
[6]	Split ring resonator / No /No	①Wi-Fi 2.4G 2x2 MIMO	19²*π*7.5	No	No	No	BT/WIFI applications	Yes
[7]	Theory of Characteristic Modes/ No /No	①Wi-Fi 2.4G 2x2 MIMO	18²*π*7.5	No	No	No	Biomedical healthcare monitoring	No
[8]	Shared-Slots, IFA, Loop, Shared Radiators/Yes /Yes	①LTE M/HB ②GPS 1575, ③Wi-Fi 2.4G④GSM 850/900	43.6*43.6*5.8	No	No	Yes	Medical and telemetry with implanted device	No
[9]	IFA antenna/Yes /No	LTE B1/B2/B3/B4/B13	44*44*10	No	No	No	Medical Implant Communication Service	No
[10]	Metal belt for monopole and dipole antenna/No /Yes	700MHz,1.7GHz~2.7GHz	40*40*35	No	No	No	BT/WIFI applications	Yes
[16]	Loop antenna / Yes/ No	②GPS 1575③Wi-Fi 2.4/5G	40*40*π	No	No	No (On arm)	BT/WIFI applications	No
[24]	Differentially fed of loop antenna / Yes/ No	③Wi-Fi 2.4/5G	19.2*39.2*2.6	No	No	No	4G LTE	No
[25]	Partial slotted ground/Yes /No	4.0~7.2GHz	40*20*4	No	No	Yes	BT/WIFI applications	No
[26]	spiral shape planar inverted-F antenna / No /No	①Wi-Fi 2.4G 402~405MHz	25*25*π	No	No	No	GPS, BT/WIFI applications	No
[27]	chip antenna / No /No	①Wi-Fi 2.4/5G	35*25*10	No	No	Yes	BT/WIFI applications	No
[28]	Electromagnetic bandgap / No /No	24GHz	19.04*15.06	No	Yes	Yes	On body applications	Yes
[29]	Circularly polarized (CP) MIMO antenna/ No /No	①Wi-Fi 2.4G,	40*40*1.6	No	Yes	No (On arm)	wearable biotelemetric devices	Yes
[30]	Semi-exible antenna / No /No	①Wi-Fi 2.4G	17*25*0.787	No	No	No (On arm)	biomedical telemetry applications	Yes
[31]	Metasurface antenna/ No /No	Wi-Fi 5G	42*28*4	No	No	No (On arm)	Textile material wearable application	Yes
[32]	Robust Flexible Wearable Antenna/ No /No	①Wi-Fi 2.4G	77*47*2.7	No	No	No	BT/WIFI applications	No
[33]	C-shape etching slot antenna/ No /No	3.3–3.8 GHz, 4.5–5.5 GHz	18*19*1	No	No	No	various substrates for Wi-MAX applications	Yes
[34]	180 nm CMOS Low-Power Transmitter / No /No	①Wi-Fi 2.4G	2.3*5*0.001	No	No	No	wireless charging of IoT	No
[35]	Dual circular patch / No /No	①Wi-Fi 2.4G	40*40*1.6	No	No	Yes	Human tissue sensing	No
[36]	Reconfigurable wearable textile antenna/ No /No	1.82–3.79 GHz	60*50*3.2	No	No	No	biomedical applications	No
[37]	Shorting Strategies antenna/Yes /No	③Wi-Fi 2.4/5G	60*40*3.2	No	No	No	buttons textile applications	No
[38]	Circularly Polarized Patch Antenna ´/ No /No	0.915 GHz	50*50*4.5	No	No	No	wearable systems	No
[39]	Dual-band folded-ring antenna/ No /No	①Wi-Fi 2.4G, 3.4-3.6GHz	60*60*4.2	No	No	No (On arm)	off-body communication	Yes
This work	Integrate and Coupled Metal Frame, Share-Slot, Loop, Slot, Bandpass filter/Yes /Yes /Yes / Yes	①5G n77/78/79 band 2x2 MIMO ②GPS 1575 ③Wi-Fi 2.4/5G ④GSM 850/900	43*37*8	Yes	Yes	Yes	5G communication systems, the IoT, and Real-time location systems	Yes

FR1 n77/78/79 bands. The device proposed in this study features a 2 × 2 MIMO array and coverage of the 5G FR1 n77/78/79 band. Multiantenna pattern diversity and SAR were evaluated.

V. CONCLUSION

This paper presents an antenna system for wearable devices that has potential for use in 5G and IoT applications. The electromagnetic shielding problem caused by the metal frame and metal strap of the smart watch was resolved. The frequency bands covered were WLAN 2.4-GHz/5-GHz channels (2410–2484 MHz), GPS (1575 MHz), narrowband IoT band 8 (880–915 MHz), GSM 850/900, and the 5G FR1 n77/78/79 band (3300–5000 MHz). The mutually reinforcing performance of the metal strap and the antenna system was discussed. Notably, a diversity effect was achieved with regard to radiation pattern. For the installation of the 2 × 2 MIMO arrays in the narrow device, the envelope correlation coefficients were all less than 0.1. The SAR was examined in the context of wearable devices and hand tissue. Our results are in line with commercial standards and international norms. Regarding overall frequency band contributions, the coupled frame radiation, slot mode, loop mode, and matching network were integrated. The performance of the MIMO array was evaluated, and the DG and multiplexing efficiency were imported into the proposed antenna values; the results were excellent. Finally, the channel capacity of the 5G FR1 n77/78/79 frequency band was calculated, reaching 76.5% of the theoretical upper limit, in line with the requirements for improving the spectrum efficiency. Thus, our antenna system can be employed in applications involving 5G communication systems, the IoT, and RTLS.

REFERENCES

[1] D. Wu and S. W. Cheung, "A cavity-backed annular slot antenna with high efficiency for smartwatches with metallic housing," *IEEE Trans. Antennas Propag.*, vol. 65, no. 7, pp. 3756–3761, Jul. 2017.
[2] S.-W. Su and Y.-T. Hsieh, "Integrated metal-frame antenna for smartwatch wearable device," *IEEE Trans. Antennas Propag.*, vol. 63, no. 7, pp. 3301–3305, Jul. 2015.
[3] Z. Duan and L.-J. Xu, "Dual band wristband antenna with metal frame loaded for biomedical applications," *Microw. Opt. Technol. Lett.*, vol. 59, no. 9, pp. 2155–2159, Sep. 2017.
[4] C.-H. Wu, K.-L. Wong, Y.-C. Lin, and S.-W. Su, "Internal shorted monopole antenna for the watch-type wireless communication device for Bluetooth operation," *Microw. Opt. Technol. Lett.*, vol. 49, pp. 942–946, Apr. 2007.
[5] D. Wu, S. W. Cheung, Q. L. Li, and T. I. Yuk, "Slot antenna for all-metal smartwatch applications," in *Proc. 10th Eur. Conf. Antennas Propag. (EuCAP)*, Davos, Switzerland, Apr. 2016, pp. 1–4.
[6] B. Wang and S. Yan, "Design of smartwatch integrated antenna with polarization diversity," *IEEE Access*, vol. 8, pp. 123440–123448, 2020.
[7] D. Wen, Y. Hao, H. Wang, and H. Zhou, "Design of a MIMO antenna with high isolation for smartwatch applications using the theory of characteristic modes," *IEEE Trans. Antennas Propag.*, vol. 67, no. 3, pp. 1437–1447, Mar. 2019.
[8] C. Chen, Y. Lin, P. Huang, H. Chen, and C. Liao, "Design of multi-band antenna for LTE wearable device with shared slots and radiators for smart watch," *Int. J. RF Microw. Comput.-Aided Eng.*, vol. 30, no. 11, Nov. 2020, Art. no. e22415.
[9] S.-W. Su and Y.-T. Hsieh, "Integrated LDS antenna for B13 and B4/B3/B2/B1 LTE operation in smartwatch," *Microw. Opt. Technol. Lett.*, vol. 59, no. 4, pp. 869–873, Apr. 2017.
[10] K. Zhao, Z. N. Ying, and S. L. He, "Antenna designs of smart watch for cellular communications by using metal belt," in *Proc. 9th Eur. Conf. Antennas Propag. (EuCAP)*, Lisbon, Portugal, 2015, pp. 1–5.
[11] H. Chen and A. Zhao, "LTE antenna design for mobile phone with metal frame," *IEEE Antennas Wireless Propag. Lett.*, vol. 15, pp. 1462–1465, 2016.
[12] D. Huang and Z. Du, "Eight-band antenna with a small ground clearance for LTE metal-frame mobile phone applications," *IEEE Antennas Wireless Propag. Lett.*, vol. 17, no. 1, pp. 34–37, Jan. 2018.
[13] H.-J. Chang and K.-L. Wong, "Compact LTE frame antenna with a narrow metal clearance and a radiating feed network for the metal-casing smartphone," in *Proc. 11th Eur. Conf. Antennas Propag. (EUCAP)*, Mar. 2017, pp. 3069–3073.
[14] Y. Liu, W. Cui, Y. Jia, and A. Ren, "Hepta-band metal-frame antenna for LTE/WWAN full-screen smartphone," *IEEE Antennas Wireless Propag. Lett.*, vol. 19, no. 7, pp. 1241–1245, Jul. 2020.
[15] D. Huang, Z. Du, and Y. Wang, "A quad-antenna system for 4G/5G/GPS metal frame mobile phones," *IEEE Antennas Wireless Propag. Lett.*, vol. 18, no. 8, pp. 1586–1590, Aug. 2019.
[16] M. Jeon, W. C. Choi, and Y. J. Yoon, "GPS, Bluetooth and Wi-Fi tri-band antenna on metal frame of smartwatch," in *Proc. IEEE Int. Symp. Antennas Propag. (APSURSI)*, Jun. 2016, pp. 2177–2178.
[17] D. Huang and Z. Du, "Compact wideband MIMO antenna system for 5G metal frame mobile phones," in *Proc. Int. Appl. Comput. Electromagn. Soc. Symp. China (ACES)*, Aug. 2019, pp. 1–2.
[18] H. Tu, Y. He, W. Li, W. He, and A. Boag, "A multi-band metal-rimmed antenna for 5G smartphones," in *Proc. IEEE Asia–Pacific Microw. Conf. (APMC)*, Dec. 2020, pp. 755–757.
[19] H. Li, Y. Cheng, L. Mei, and F. Wu, "Dual-polarized frame-integrated slot arrays for 5G mobile handsets," *IEEE Antennas Wireless Propag. Lett.*, vol. 19, no. 11, pp. 1953–1957, Nov. 2020.
[20] K.-L. Wong and C.-Y. Tsai, "IFA-based metal-frame antenna without ground clearance for the LTE/WWAN operation in the metal-casing tablet computer," *IEEE Trans. Antennas Propag.*, vol. 64, no. 1, pp. 53–60, Jan. 2016.
[21] C.-Y. Tsai and K.-L. Wong, "Inverted-F antenna-based on-frame GPS/WLAN antenna for the metal-casing tablet computer," in *Proc. 10th Eur. Conf. Antennas Propag. (EuCAP)*, Apr. 2016, pp. 1–4.
[22] K. Wong, C. Tsai, and P. Wu, "Dual-wideband open-slot antennas with two open ends for the LTE metal-framed tablet device," in *Proc. Int. Symp. Antennas Propag. (ISAP)*, 2015, pp. 1–4.
[23] L. Chen, Y. Wu, and K. Wong, "Triple-wideband inverted-F frame antenna for the LTE metal-casing smartphone," in *Proc. 11th Eur. Conf. Antennas Propag. (EUCAP)*, 2017, pp. 3064–3068.
[24] L.-J. Xu and Z. Duan, "Differential wide band metal-frame antenna for wristband applications," in *IEEE MTT-S Int. Microw. Symp. Dig.*, Chengdu, China, Jul. 2016, pp. 1–3.
[25] Z. Duan, L. Xu, and W. Geyi, "Metal frame repeater antenna with partial slotted ground for bandwidth enhancement of wristband devices," *IET Microw., Antennas Propag.*, vol. 11, no. 10, pp. 1438–1444, Aug. 2017.
[26] H. Hamouda, P. L. Thuc, R. Staraj, and G. Kossiavas, "Small antenna embedded in a wrist-watch for application in telemedicine," in *Proc. 8th Eur. Conf. Antennas Propag. (EuCAP)*, Hague, The Netherlands, Apr. 2014, pp. 876–879.
[27] S. Sojuyigbe and K. Daniel, "Wearables/IOT devices: Challenges and solutions to integration of miniature antennas in close proximity to the human body," in *Proc. IEEE Symp. Electromagn. Compat. Signal Integrity*, Santa Clara, CA, USA, Mar. 2015, pp. 75–78.
[28] A. Iqbal, A. Basir, A. Smida, N. K. Mallat, I. Elfergani, J. Rodriguez, and S. Kim, "Electromagnetic bandgap backed millimeter-wave MIMO antenna for wearable applications," *IEEE Access*, vol. 7, pp. 111135–111144, 2019.
[29] A. Iqbal, A. Smida, A. J. Alazemi, M. I. Waly, N. K. Mallat, and S. Kim, "Wideband circularly polarized MIMO antenna for high data wearable biotelemetric devices," *IEEE Access*, vol. 8, pp. 17935–17944, 2020.
[30] A. Smida, A. Iqbal, A. J. Alazemi, M. I. Waly, R. Ghayoula, and S. Kim, "Wideband wearable antenna for biomedical telemetry applications," *IEEE Access*, vol. 8, pp. 15687–15694, 2020.

[31] S. Ahmed, D. Le, L. Sydänheimo, L. Ukkonen, and T. Björninen, "Wearable metasurface-enabled quasi-yagi antenna for UHF RFID reader with end-fire radiation along the forearm," *IEEE Access*, vol. 9, pp. 77229–77238, 2021.

[32] F. E. Rahmad, S. Y. Mohamad, N. F. A. Malek, F. A. Rahman, A. A. Ruslan, and N. Zainal, "Development of rubber substrate for more robust flexible wearable antenna at 2.4 GHz application," in *Proc. 8th Int. Conf. Comput. Commun. Eng. (ICCCE)*, Jun. 2021, pp. 150–155.

[33] M. M. H. Mahfuz, M. R. Islam, N. Sakib, M. H. Habaebi, R. Raad, and M. A. T. Sakib, "Design of wearable textile patch antenna using C-shape etching slot for Wi-MAX and 5G lower band applications," in *Proc. 8th Int. Conf. Comput. Commun. Eng. (ICCCE)*, Jun. 2021, pp. 168–172.

[34] A. Hejazi, B. Jang, R. E. Rad, J. W. Jo, B. S. Rikan, Y. Pu, S.-S. Yoo, K. C. Hwang, Y. Yang, and K.-Y. Lee, "A 2.4 GHz power receiver embedded with a low-power transmitter and PCE of 53.8%, for wireless charging of IoT/wearable devices," *IEEE Trans. Microw. Theory Techn.*, early access, Jun. 25, 2021, doi: 10.1109/TMTT.2021.3088503.

[35] W. Saadat, S. A. Raurale, G. A. Conway, and J. McAllister, "Wearable antennas for human identification at 2.45 GHz," *IEEE Trans. Antennas Propag.*, early access, Jun. 25, 2021, doi: 10.1109/TAP.2021.3090852.

[36] Q. H. Dang, S. J. Chen, D. C. Ranasinghe, and C. Fumeaux, "A frequency-reconfigurable wearable textile antenna with one octave tuning range," *IEEE Trans. Antennas Propag.*, early access, Jun. 2, 2021, doi: 10.1109/TAP.2021.3083826.

[37] Q. H. Dang, S. J. Chen, B. Zhu, and C. Fumeaux, "Shorting strategies for wearable textile antennas: A review of four shorting methods," *IEEE Antennas Propag. Mag.*, early access, May 4, 2021, doi: 10.1109/MAP.2021.3073152.

[38] D. Le, S. Ahmed, L. Ukkonen, and T. Björninen, "A small all-corners-truncated circularly polarized microstrip patch antenna on textile substrate for wearable passive UHF RFID tags," *IEEE J. Radio Freq. Identificat.*, vol. 5, no. 2, pp. 106–112, Jun. 2021.

[39] T. Le and T.-Y. Yun, "Wearable dual-band high-gain low-SAR antenna for off-body communication," *IEEE Antennas Wireless Propag. Lett.*, vol. 20, no. 7, pp. 1175–1179, Jul. 2021.

[40] G. J. Foschini and M. J. Gans, "On limits of wireless communications in a fading environment when using multiple antennas," *Wireless Pers. Commun.*, vol. 6, pp. 311–335, Mar. 1998.

[41] K.-L. Wong, C.-Y. Tsai, and J.-Y. Lu, "Two asymmetrically mirrored gap-coupled loop antennas as a compact building block for eight-antenna MIMO array in the future smartphone," *IEEE Trans. Antennas Propag.*, vol. 65, no. 4, pp. 1765–1778, Apr. 2017.

[42] M. Koohestani, A. Hussain, A. A. Moreira, and A. K. Skrivervik, "Diversity gain influenced by polarization and spatial diversity techniques in ultrawideband," *IEEE Access*, vol. 3, pp. 281–286, 2015.

[43] X. Chen, "Throughput multiplexing efficiency for MIMO antenna characterization," *IEEE Antennas Wireless Propag. Lett.*, vol. 12, pp. 1208–1211, 2013.

[44] X.-T. Yuan, W. He, K.-D. Hong, C.-Z. Han, Z. Chen, and T. Yuan, "Ultra-wideband MIMO antenna system with high element-isolation for 5G smartphone application," *IEEE Access*, vol. 8, pp. 56281–56289, 2020.

[45] P. A. Hasgall et al., "IT'IS database for thermal and electromagnetic parameters of biological tissues, version 4.0," May 2018.

[46] K.-L. Wong, H.-J. Chang, C.-Y. Wang, and S.-Y. Wang, "Very-low-profile grounded coplanar waveguide-fed dual-band WLAN slot antenna for on-body antenna application," *IEEE Antennas Wireless Propag. Lett.*, vol. 19, no. 1, pp. 213–217, Jan. 2020.

[47] F. Foroutan and N. Noori, "SAR calculation of a pregnant woman model exposed to LTE and Wi-Fi signals," in *Proc. 10th Int. Symp. Telecommun. (IST)*, Dec. 2020, pp. 207–210.

CHIA-TE LIAO received the B.S. degree in aviation and communication electronics from the Air Force Institute of Technology, Taiwan, in 2005, the M.S. degree from the Institute of Electrical Engineering, Donghua University, in 2011, and the Ph.D. degree in electronic engineering from the National Kaohsiung University of Applied Sciences, Taiwan, in 2017. Since 2011, he has been with the Aviation Communication and Electronics, Air Force Institute of Technology. He is currently an Assistant Professor and the Director of the Department of Aero-Electronics Engineering, in 2020. His research interests include RFID antennas, MIMO antennas, and radio electromagnetic modeling. He has won the Mobile Heroes Communication Contest Championship and the Jury Special Award from Taiwan, in 2016 and 2017.

ZHE-KAI YANG received the B.S. degree from the Department of Electro-Optical Engineering, Southern Taiwan University of Science, in 2019, and the M.S. degree from the Institute of Photonics and Communications, National Kaohsiung University of Science and Technology, Taiwan, in 2021. He is currently working at the RF Communication of COMPAL Electronic, INC. His research interests include smart watch antennas, MIMO antennas, metal frame antennas, and 4G/5G terminal device antennas. He has been awarded the Best Student Paper Award in the 2020 Conference on Photonics and Communications.

HUA-MING CHEN (Senior Member, IEEE) received the B.S. degree in physics from the National Tsing Hua University, Hsinchu, Taiwan, in 1983, the M.S. degree in electro-optics from the National Chiao Tung University, Hsinchu, in 1987, and the Ph.D. degree in electrical engineering from the National Sun Yat-sen University, Kaohsiung, Taiwan, in 1996. Since 1988, he has been with the Institute of Photonics and Communications, National Kaohsiung University of Applied Sciences, Kaohsiung, where he became a Professor, in 2001, where he also served as the Director of the Institute of Photonics and Communications, from 2005 to 2008. He is currently a Distinguished Professor and the Director of the Institute of Photonics Engineering. He has authored more than 110 journal and conference papers and takes out 20 patents on antenna design. Several of his antenna designs have been licensed to industry for production. His research interests include antennas for smart connected devices, dielectric resonator antennas, RFID antennas, and microwave filter design.

He was elected as the President of the Institute of Antennas Engineers of Taiwan (IAET), from 2010 to 2012. He was also elected as the Chair of the IEEE AP-S Tainan Chapter, from 2009 to 2010. He served as the Publications Committee Chair for ISAP 2014, and the International Technical Program Committee Member of the IEEE AEM2C 2010 and the IEEE iWEM 2011 in Taiwan. He was also listed in Who's Who in Science and Engineering and Who's Who in Asia. He served as Trustees for the IEEE Tainan Section (2010–2011) and the Chinese Microwave Association (2009–2011). He was a recipient of the IEEE 2011 Best Chapter Award.

• • •